Title

Equilibrium and Non-equilibrium Complex Fragment Emission in 50-100 Me V/u {sup 139}La + {sup 12}C Reactions

Journal

Nuclear physics A, 523

Authors

Bowman, D.R.
Peaslee, G.F.
Colonna, N.
et al.

Publication Date

1990-02-01

LBL-28371
Preprint

Lawrence Berkeley Laboratory
UNIVERSITY OF CALIFORNIA

Submitted to Nuclear Physics A

Equilibrium and Non-equilibrium Complex Fragment Emission in 50 – 100 MeV/u $^{139}La + ^{12}C$ Reactions

D.R. Bowman, G.F. Peaslee, N. Colonna,
R.J. Charity, M.A. McMahan, D. Delis,
H. Han, K. Jing, G.J. Wozniak, and
L.G. Moretto

February 1990

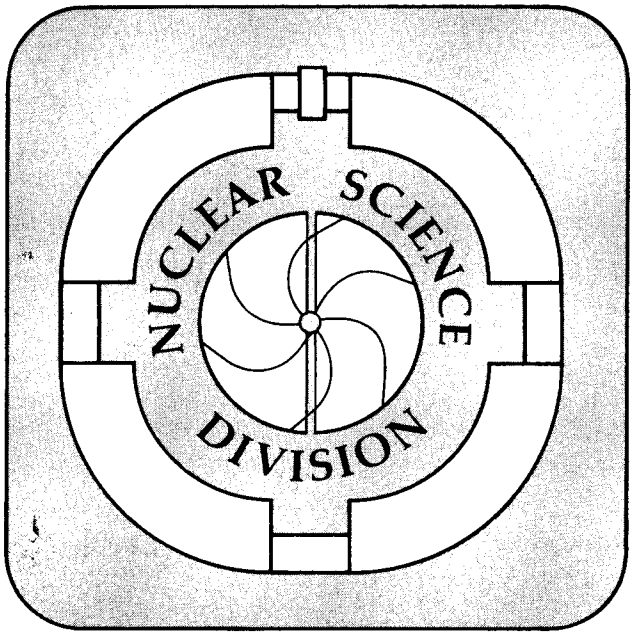

Prepared for the U.S. Department of Energy under Contract Number DE-AC03-76SF00098.

DISCLAIMER

LBL - 28371

Equilibrium and Non-equilibrium Complex Fragment Emission in 50 - 100 MeV/u $^{139}La + ^{12}C$ Reactions

D.R. Bowman, G.F. Peaslee, N. Colonna, R.J. Charity, M.A. McMahan,
D. Delis, H. Han, K. Jing, G.J. Wozniak, and L.G. Moretto

Nuclear Science Division, Lawrence Berkeley Laboratory
1 Cyclotron Road, Berkeley, CA 94720

February 1990

This work was supported by the Director, Office of Energy Research, Division of Nuclear Physics of the Office of High Energy and Nuclear Physics of the U.S. Department of Energy under Contract DE-AC03-76SF00098

Equilibrium and Non-equilibrium Complex Fragment Emission in 50 - 100 MeV/u $^{139}La + ^{12}C$ Reactions*

D.R. BOWMAN[1], G.F. PEASLEE, N. COLONNA, R.J. CHARITY[2], M.A. McMAHAN, D. DELIS, H. HAN[3], K. JING[3], G.J. WOZNIAK, and L.G. MORETTO

Nuclear Science Division, Lawrence Berkeley Laboratory, 1 Cyclotron Road, Berkeley, CA 94720

W.L. KEHOE[4], B. LIBBY, and A.C. MIGNEREY

Department of Chemistry, University of Maryland, College Park, MD 20742

A. MORONI, S. ANGIUS, and I. IORI

INFN and Department of Physics, University of Milano, Via Celoria 16, Milan 20133, Italy

A. PANTALEO and G. GUARINO

INFN, Bari 70126, Italy

ABSTRACT:

Complex fragment emission ($Z > 2$) has been studied in the reactions of 50, 80, and 100 MeV/u $^{139}La + ^{12}C$. Charge, angle, and energy distributions were measured inclusively and in coincidence with other complex fragments, and were used to extract the source rapidities, velocity distributions, and cross sections. The binary signature of the coincidence events and the sharpness of the velocity distributions illustrate the primarily 2-body nature of these reactions. Calculations based on statistical compound nucleus decay have been compared with the experimental data. The emission velocities, angular distributions, and absolute cross sections of fragments of $20 \leq Z \leq 35$ at 50 MeV/u, $19 \leq Z \leq 28$ at 80 MeV/u, and $17 \leq Z \leq 21$ at 100 MeV/u are consistent with the binary decay of compound nuclei formed in incomplete fusion reactions in which the ^{139}La projectile picks up about one-half of the ^{12}C target. At 80 and 100 MeV/u, statistical model calculations are also able to reproduce the isotropic portion of the cross section for lighter and heavier fragments. However, a significant fraction of the total cross section for these fragments is due to non-equilibrium emission. Although the emission process is still mainly binary, and the relative velocity between the fragments is determined by their mutual Coulomb repulsion, the anisotropic angular distributions and the magnitudes of the absolute yields are incompatible with standard compound-nucleus statistical decay.

1. Introduction

Complex fragment ($Z > 2$) emission in intermediate energy nuclear reactions has been a subject of both experimental and theoretical interest for many years[1,2]). The first studies of this process[3-7]) identified two components: a fast, non-equilibrium component producing light fragments at forward angles, and a relaxed component producing heavy fragments at all angles and light fragments at backward angles.

The non-equilibrium component is characterized by mass or charge distributions following a power-law[4]), by Maxwellian energy spectra with slope "temperatures" dependent upon fragment mass[5,7]), and by forward peaked angular distributions[4,6]). The cross sections for this process become a larger fraction of the total complex fragment yield as the bombarding energy is increased from 20 to 50 MeV/u[8]). It has been shown recently in the 27 MeV/u $^{40}Ar + {}^{nat}Ag$ reaction that the non-equilibrium fragments are emitted in binary reactions, and that the fragments are produced with both complete and incomplete energy relaxation over a large angular region[9]). In this reaction, these fragments were attributed to deep-inelastic and quasi-elastic reactions. Other mechanisms proposed to account for the non-equilibrium complex fragments include a liquid-gas phase transition in the nuclear medium[10]), a non-equilibrim statistical emission model[7]), a cold shattering of the nucleus[11]), and a coalescence of nucleons[12]).

A systematic study of the relaxed component at low bombarding energy demonstrated the compound nucleus nature of the emission process[6,13,14]). The excitation functions for the equilibrium emission of fragments of $3 \leq Z \leq 11$ illustrate the opening of phase space with increasing excitation energy[14]). These excitation functions are reminiscent of fission excitation functions[15]), and are in excellent agreement with theoretical predictions based on a transition state formalism of complex fragment (CF) decay[16,17]).

The process of CF emission from excited compound nuclei has been systematically studied for asymmetric entrance channels (X + Al, C, Be) throughout the periodic table, from 8 MeV/u, where the process is very rare, up to 40 MeV/u, where the CF emission probability can approach unity[6,13,14,18-25]). For these asymmetric entrance channels, a large range of impact parameters gives rise to complete geometric overlap between the target and the projectile. In addition, the interplay of the complex fragment emission probability with excitation energy and angular momentum determines that, even in incomplete fusion reactions, most of the fragments arise from a limited range of impact parameters[21]). Hence, it has been shown that the complex fragments are emitted from a source with a sharply defined velocity, and that the reactions can be characterized from the inclusive data alone.

In reactions with very asymmetric entrance channels (X + C, Be), the fragments with masses between the projectile and target originate solely from the binary decay of equilibrated compound nuclei. This conclusion has been reached based upon the analysis of source velocities, emission velocities, angular distributions, the direct measurement of the binary nature of the process, and, above all, by the shape of the charge distributions and the magnitude of the cross sections as a function of excitation energy. For more symmetric entrance channels (X + Al), the isotropic cross section increases substantially and an additional source of complex fragments may be required[22]).

As the bombarding energy is increased, the compound nuclei result from progressively less extensive fusion of the target and projectile, in agreement with linear-momentum transfer systematics[26-30]).

In order to test whether the incomplete-fusion compound-nucleus statistical-decay model can also explain much of the CF emission at larger bombarding energies, we have studied the very asymmetric $^{139}La + ^{12}C$ system at 50, 80 and 100 MeV/u. A previous study of evaporation residues speculated about the disappearance of the fusion and incomplete fusion processes above 27 MeV/u[31]). However, it has since been demonstrated for lighter systems at these energies that complex fragment emission can be a more sensitive probe for fusion or incomplete fusion products[24]).

Two interesting questions are relevant to the extension of these studies to larger bombarding energies:

1) What is the maximum relative velocity beyond which there is no longer capture of any portion of the target nucleus by the projectile? That is, at what bombarding energy does the incomplete fusion process, which is well established at low energy[26-30]), cease to be a good model of nuclear interactions?

2) What is the maximum excitation energy per nucleon that a nucleus can thermalize? Or equivalently, what is the limiting temperature above which fully equilibrated compound nuclei are no longer formed?

The maximum relative velocity that can sustain incomplete fusion should depend upon the impact parameter and the target-projectile combination[32]). Above a threshold bombarding energy, the incomplete fusion process should give way to the participant-spectator mechanism observed at higher energy[33-35]).

The maximum possible excitation energy that a nucleus can hold is related to the critical temperature. Bulk disintegration models predict a prompt multifragmentation of the nucleus, at excitation energies[36]) substantially lower than the total binding energy. As the bombarding energy increases, multifragment emission is expected to become an important deexcitation mode . This multifragment decay may be due to a prompt nuclear disintegration, or instead, it could be due to a classical compound nucleus undergoing a series of binary decays. If this multifragment emission is governed by a statistical mechanism, such as compound nucleus decay, then the important

parameter is the nuclear temperature. If, however, the mechanism is dynamic, then the bombarding energy may be the quantity of interest. Recent work has indicated that the excitation energy of the system, rather than the bombarding energy, is more strongly correlated to the complex fragment multiplicity [37-39]).

This paper is organized as follows: the experimental details are given in section 2; the experimental results are presented and discussed in section 3; model calculations are compared with the data in section 4; and the conclusions are presented in section 5. A portion of this work has been previously published[40]).

2. Experimental

These experiments take advantage of the unique heavy beam capabilities of the Lawrence Berkeley Laboratory BEVALAC by using reverse kinematics, in which the heavier nucleus (^{139}La) is used as the projectile. The resulting large laboratory velocities of the heavy reaction products allow them to be identified easily with E - ΔE telescopes. With normal kinematics (light beams on heavy targets), a large fraction of the cross section associated with these heavy fragments have energies below typical detector thresholds. Reverse kinematics also gives rise to a forward focusing of the reaction products. As a consequence, modest sized detectors have large efficiencies. This effect is particularly important for detecting coincident fragments.

2.1 50 MeV/u ^{139}La + ^{12}C REACTION

A 50 MeV/u ^{139}La beam impinged upon a self-supporting ^{12}C target of 2.2 mg/cm^2 thickness. Reaction products were detected in two ΔE - E detector telescopes centered at 5.5^o on either side of the beam. The telescopes subtended a solid angle of 5.9 msr, covering from 3^o - 8^o in-plane and $\pm$2.5^o out-of-plane. Although this solid angle is not particularly large, the focusing of the reaction products due to reverse kinematics allowed for reasonable detection efficiencies for both inclusive (10 % for Z = 25) and coincidence (3 % for Z = 25) events.

Fragments striking the telescope were identified by their energy loss (ΔE) in a gas ionization chamber pressurized with 200 torr of a P-10 gas mixture, and their residual energy in a 2 mm thick Si(Li) detector. The telescopes were position-sensitive both in- and out-of-plane. The in-plane positions were determined from resistive-charge division across the front face of the Si(Li) detectors. The out-of-plane positions were determined by the electron drift time in the ionization chambers.

The energy calibrations of the ion chambers and the Si(Li) detectors were obtained with gas-in and gas-out runs using elastically scattered 50 MeV/u ^{139}La ions from a ^{197}Au target. Corrections for the energy losses in the targets, the 4.7 mg/cm^2 Pb foils (used for electron suppression), and the 175 μg/cm^2 mylar gas windows, along with a correction for the pulse-height deficit (PHD)[41]) in the Si(Li) detectors, were performed for the calibration beam and for each detected fragment. The energy calibration was estimated to be accurate to approximately 2%, but systematic errors in the PHD parameterization could make the absolute error larger, since this parameterization was determined at low energies and may not be accurate for ^{139}La ions at these energies.

The absolute position calibrations were performed by placing position masks with 2 mm diameter holes in front of each of the ion chambers. The theoretical position resolution was

approximately ±1 mm or 0.1°. However, the actual uncertainty in the measured angles was about ±0.8° due to the beam-spot size and beam divergence.

The beam current was monitored using a Faraday cup and a current integrator. The current integrator electronics was calibrated by delivering a known current into the preamplifier. Since the Faraday cup itself could not be calibrated with elastic scattering, the systematic error in the absolute beam intensity may be as large as 50 %.

The charge of each fragment was determined by its position in a ΔE - E matrix. The masses corresponding to a given charge were calculated from the empirical formula given in reference 40.

2.2 80 AND 100 MeV/u ^{139}La + ^{12}C REACTIONS

In these reactions, 80 and 100 MeV/u ^{139}La beams impinged upon self-supporting ^{12}C targets of 3.7 mg/cm^2 thickness. A detector array of eleven telescopes[42]) was close-packed about the beam in a 3 x 4 rectangular geometry, with one of the center positions missing for the beam exit. Each element in the array was positioned 91 cm from the target, and had a solid angle of 2.4 msr. The total array covered approximately -5° to +9° in-plane and ±5° out-of-plane, with a ±2.2° gap in- and out-of-plane about 0°.

Each detector telescope had four elements; a 300 μm thick Si detector used as a ΔE, followed by two 5 mm thick Si(Li) detectors, and finally a 7.6 cm thick plastic scintillator. The detector elements were 5.5x5.7 cm^2 in cross section, and had an square active areas of 4.5x4.5 cm^2. Each Si or Si(Li) detector was position-sensitive in one dimension. As above, the fragment positions were determined from resistive-charge division across one face of the detectors. However, these devices have resistive division in 14 discrete steps[42]), and are self-calibrating (no absolute position mask is necessary). The position-sensitive dimensions of the Si and Si(Li) detectors were arranged orthogonally to each other in order to obtain both in- and out-of-plane positions.

The energy calibrations were determined from calibration beams of 80 MeV/u ^{4}He, ^{20}Ne, ^{40}Ca, ^{139}La, and 100 MeV/u ^{139}La. Corrections for the energy losses in the target and in the 1.5 mg/cm^2 ^{197}Au foils (used for electron suppression) were applied. A new correction for the PHD was developed[43]) based on calibration data taken from 8.75 - 100 MeV/u with beams of Z = 20 - 57. This new parameterization predicts the PHD in the range of $1 \leq Z \leq 57$ to < 10%, corresponding to an uncertainty of less than 1% in total (measured + PHD) energy.

For a point source, the position resolution of these detectors was ±1.5 mm or 0.1°. For the 10 mm beam-spot, the experimental uncertainty in the angular position was ±0.3°.

A gas ionization chamber was used during the experiment to monitor the beam current. Following the experiment, the ion chamber was calibrated against the absolute beam intensity with a plastic scintillator. The systematic uncertainty in the absolute beam monitoring was estimated to be 20%.

As above, the charge of each fragment was determined by its position in a ΔE - E matrix. The masses corresponding to a given charge were estimated using the parameterization[19]) $A = 2.08\ Z + 0.0029\ Z^2$.

3. Results and Discussion

We will begin the discussion of the $^{139}La + ^{12}C$ reactions by examining some global results that illustrate the nature of the reaction mechanism. Next, we will turn to the more quantitative results: source rapidities, emission velocities, angular distributions and cross sections. Finally, we will investigate the coincidence data in some detail. Throughout the discussion, we will often compare the 50 -100 MeV/u $^{139}La + ^{12}C$ reactions to results from the same system at lower energy[25]) (14 and 18 MeV/u).

3.1 TWO-FOLD COINCIDENCE EVENTS

Important information about the reaction mechanism can be obtained by examining the two-fold complex fragment coincidence data. Plots of Z_1 versus Z_2 and $Z_1 + Z_2$ distributions tell us whether the reaction proceeds through final states with only two main fragments, or whether the exit channel is predominantly multibody. In the former case we expect that the coincidence charge distributions should peak at values near the total target plus projectile charge. In contrast, for multibody decay, where only two fragments are detected, we expect the charge distribution to be peaked, if at all, at values significantly less than the total charge in the entrance channel.

Linear contour plots of the two-fold (Z_2 versus Z_1) coincidence events at 18[25]), 50, 80 and 100 MeV/u are shown in Figure 1. At bombarding energies ≤ 50 MeV/u, the two detectors were placed symmetrically about the beam. At the higher energies the detector configuration was asymmetric. For purposes of comparison, the Z_1 - Z_2 data from the 80 and 100 MeV/u reactions have been reflected about the line $Z_1 = Z_2$.

The dashed lines in this figure indicate the total charge of the projectile plus target. The figure is striking because, at all bombarding energies, even at 100 MeV/u, the contour plots are dominated by a band of events in which two, and only two, fragments contain the bulk of the charge. This band broadens and shifts towards a smaller total charge as the bombarding energy increases. Multibody events with only two detected heavy fragments fall below the dominant band and such events become visible only at the highest bombarding energies.

The two-body nature of the process is also illustrated by the Z_{Total} ($Z_1 + Z_2$) distributions shown in Figure 2. The total charge distributions show a well defined peak that moves to smaller values with increasing bombarding energy. The tail at smaller total charge, which becomes more

evident at the higher energies, is due to multibody events in which only two of the fragments were detected.

Events in which the bulk of the target and projectile mass is contained in two heavy fragments preserve two-body kinematics. Although the reactions are not strictly binary in the sense that there is some missing mass, they can still be considered binary in the same way as are low energy fission and deep-inelastic reactions. In these processes, there are two heavy final fragments moving relative to one another with a well-defined velocity determined mainly by the Coulomb repulsion energy between the fragments. The emission of light particles either preceding or following the main binary decay acts mainly to perturb the sharpness of the relative velocity distribution.

3.2 VELOCITY DIAGRAMS

The velocity distributions of the complex fragments can also indicate the character of the reaction mechanism. If a compound nucleus is formed in a complete or incomplete fusion reaction and then undergoes binary decay, the fragments will be emitted with well-defined Coulomb velocities. (Of course, in the laboratory frame this sharp emission velocity distribution must be folded into the source velocity distribution, which can be broad[44]) in incomplete fusion reactions.) In contrast, products from multifragment emission should have broad emission velocity distributions that depend strongly upon the relative angles at which the fragments are emitted. In order to gain understanding of the emission process, we have examined the fragment velocity distributions using Z versus velocity contour plots.

Figure 3 shows the inclusive reaction products detected at laboratory angles from 3^o - 8^o in the 50 MeV/u $^{139}La + ^{12}C$ reaction. Linear contours of the Galilean-invariant cross section $\frac{\partial^2\sigma}{v^2\partial v\partial\Omega}$ in the Z - lab velocity plane are shown. The dashed line in this figure is an experimental threshold delimiting punch-through events.

Three components are visible. The first consists of heavy fragments (Z ~ 50) moving at a well defined velocity slightly smaller than the beam velocity. These fragments are a mixture of the heavy partners from very asymmetric complex fragment decay processes and of evaporation residues that have lost their excitation energy via the emission of light particles. These heavy fragments have very small velocities in the center-of-mass system and are therefore confined to a small angular region near the beam direction and to velocities near the beam velocity.

The second component has the largest yield, and consists of light (Z < 10) complex fragments with velocities significantly smaller than that of the beam. These fragments are the lighter reaction partners in the binary non-equilibrium process discussed in the Introduction.

Between Z = 12 and 35, one observes the third component, which consists of the two ridges that merge at a velocity $V = 0.95V_{beam}$. This component has the smallest yield and is comprised of fragments produced in the binary decay of a composite system. At a single laboratory angle, two ridges in velocity arise from the emission of fragments forward and backward in the source frame. The increasing separation in laboratory velocity between the two ridges with decreasing Z-value is due to linear momentum conservation in the binary decay process that gives a larger emission velocity to the lighter fragment. The distribution of events along the two Coulomb ridges is strong evidence for the binary, relaxed nature of the process. There is no filling in of the area between the ridges as would be expected for events with higher multiplicities of complex fragments.

The continuity of these processes as a function of bombarding energy is exhibited by the similarity of the distributions obtained in the same reaction at lower bombarding energies[25]), and those in the 80 and 100 MeV/u reactions (Figs. 4 & 5). For these higher energy reactions, the Lorentz-invariant cross sections $\frac{\partial^2\sigma}{\gamma^4 v^2 \partial v \partial\Omega}$ are shown. The patterns of heavy residues, non-equilibrium light complex fragments, and Coulomb ridges characteristic of relaxed binary decay are observed at each bombarding energy. The heavy residues dominate the distributions at the smallest laboratory angles. At larger angles where the heavy residues are kinematically forbidden due to their small c.m. velocity, the non-equilibrium light complex fragments dominate.

Another way of portraying the global nature of the emission process is to plot, for a given Z-value, the cross section in velocity space as $\frac{\partial^2\sigma}{\partial v_{\|}\partial v_{\perp}}$. A schematic representation of the binary emission of complex fragments from an equilibrated source with velocity V_S is shown in Figure 6(a). The emission of complex fragments at high angular momentum appears as an isotropic Coulomb ring centered at the arrowhead. In the binary decay process each fragment also has a partner (emitted 180° apart in the source frame), located on another ring, with a radius determined by the Coulomb repulsion energy and the mass ratio of the fragments. The ring is smeared by pre-equilibrium effects (particle emission and incomplete fusion), sequential evaporation of light particles, and thermal fluctuations of the Coulomb energy[17]). The dashed lines in the figure correspond to the limits of the detector acceptance between 3.0° and 8.0° in the 50 MeV/u $^{139}La + ^{12}C$ reaction. The solid areas between these lines are the expected loci of observed events.

The experimental cross sections are presented in Figure 6(b,c,d) for Z bins of 21-23, 24-26, and 27-29. The distributions exhibit isotropic rings, strikingly similar to the schematic representation. Arrows 1 and 3 represent the beam velocity and the velocity resulting from complete fusion, respectively. The experimentally determined source velocity (see below) is indicated by arrow 2. The Coulomb rings associated with the different Z bins are centered at approximately the same value of $v_{\|}$, suggesting that all of these fragments have a common origin.

The radii of the experimental distributions correspond to the emission velocities in the source frame. These velocities decrease approximately linearly with increasing fragment charge, in accordance with the Coulomb effect. The observed independence of the source velocity upon Z-value, the decreasing emission velocity with increasing Z-value, and the angular isotropy in the reaction plane are all consistent with complex fragment emission from the binary decay of an equilibrated compound nucleus at high angular momentum.

Cross sections in the rapidity - perpendicular momentum plane $\left(\frac{\partial^2\sigma}{\partial Y\, \partial(P_\perp/mc)}\right)$ are shown in Figures 7 and 8 for representative fragments emitted in the 80 and 100 MeV/u $^{139}La + ^{12}C$ reactions. As observed at lower bombarding energies, the cross sections are distributed along Coulomb rings centered at a constant source velocity. The sharpness of the rings indicates that most of the reactions leading to these products are "quasi-binary", and that the two-body kinematics is preserved. At lower bombarding energies, the distributions along the Coulomb rings are isotropic. In contrast, at these higher energies the distributions are no longer isotropic. They evolve from backward peaked at $Z < 20$, to forward/backward symmetric around $Z = 22$, and finally to forward peaked for $Z > 26$. These anisotropic angular distributions suggest a non-equilibrium emission mechanism at higher energies.

3.3 SOURCE RAPIDITIES

It is instructive to determine the average source rapidity as a function of fragment Z-value. If all of the fragments have a common origin, the source rapidity should be independent of the fragment Z-value. If, on the other hand, a dependence is found, it may indicate that the fragments are produced by different mechanisms, or by a range of sources in an incomplete fusion process[44]).

The average source velocities were extracted from the centroids of the laboratory velocity distributions in the 50 MeV/u $^{139}La + ^{12}C$ reaction, as described in reference 21. In order to facilitate comparisons with higher energy data, these source velocities were converted to rapidities. In the lower portion of Figure 9, the ratio of the source rapidity to the beam rapidity is plotted as a function of fragment Z-value for $21 \leq Z \leq 35$. The average source rapidity appears constant over this range, indicating the common origin of all of these fragments. The solid line represents the mean source rapidity, which is intermediate between the beam (1.00) and the complete fusion (dashed line) rapidities. The small error bar for each Z-value is the statistical error associated with the extraction of the average source velocity; the large single error bar is the possible systematic error due to uncertainties in the energy calibration, and in the mass parameterization.

In order to extract source rapidities from the inclusive data at 80 and 100 MeV/u, the experimental rapidity-perpendicular momentum distributions were Lorentz-transformed into an

assumed source frame. The centroids of the emission velocity distributions in this frame were extracted as a function of the emission angle. The distributions of these centroids as a function of emission angle were then fit to ellipses. The centers of the elliptical fits determine the experimental source rapidities, and are shown as the open points in Figure 9. The need to fit the distributions to ellipses, rather than circles, is illustrated by Figure 10, in which the emission velocity in the source frame for Z = 26 fragments is plotted as a function of the emission angle in this frame. The dashed line is a least-squares fit of an ellipse to the experimental data. A circular distribution would be indicated by emission velocities that are independent of emission angle. Circular distributions, like those observed at lower energy[25]), are expected only for equilibrium emission from a well-defined source.

The source rapidity can also be obtained from the coincidence events as the center-of-mass rapidity of the fragments[44]). The coincidence source rapidity distributions, integrated over all Z-values, are shown in Figure 11 for 2-fold, 3-fold, and 4-fold events. Figure 9 shows the inclusive and coincidence source/beam rapidity ratios as a function of fragment Z-value for the 80 and 100 MeV/u $^{139}La + ^{12}C$ system. The rapidities obtained from the inclusive and the coincidence events agree within the experimental uncertainty. At 100 MeV/u the Coulomb circles were less well defined and the source rapidities were obtained over a more limited range with larger uncertainties. As at lower energy[25]), the extracted source rapidities show little dependence upon fragment Z-value.

The widths of the source rapidity and the source momentum distributions along the x and y axes (P_x and P_y) are shown in Figure 12 for the coincidence data. The width of rapidity distribution is slightly larger than the other widths and it increases more steeply with the available center-of-mass energy. This dependence accounts for the change from nearly circular to elliptical distributions with increasing bombarding energy. The momentum distributions in- and out-of-plane should, in principle, be identical. The slopes of the P_x and P_y widths are very similar, and this difference along with the slight difference in magnitude is probably due to the systematic errors introduced by the (asymmetric) detector geometry, the beam spot size, and beam divergence.

We have attempted to reproduce an elliptical rapidity - $P_\perp/mc$ distribution by assuming that a range of sources with the source rapidity distribution given in Figure 11 emits fragments with a constant emission velocity. The solid line in Figure 10 is the result of a simulation for Z = 26 fragments in the 80 MeV/u $^{139}La + ^{12}C$ reaction. This simulation indicates that the observed elliptical distributions are due to an extended source velocity distribution, rather than to an emission velocity dependence upon the emission angle.

The extracted ratio of the source to beam rapidity for both inclusive and coincidence events is shown as a function of bombarding energy in Figure 13. Within error bars, the ratios show no dependence upon bombarding energy above 50 MeV/u. The solid line is the source rapidity ratio predicted from momentum transfer systematics[26-30]). The 14, 18, and 50 MeV/u data points are in

agreement with the systematics; the 80 and 100 MeV/u data points show source rapidities smaller than the systematics (corresponding to larger momentum transfers). However, the systematics above 60 MeV/u were determined from proton energy distributions[27]). Since the barriers for complex fragment decay are much larger than for proton decay, complex fragment emission should, on the average, be associated with events with larger energy deposition. Hence, it is not surprising that the source rapidities (momentum transfers) for complex fragment emission are found to be smaller (larger) than that for proton emission.

3.4 EMISSION VELOCITIES

From the radii of the distributions in velocity space, the average emission velocity for each Z-value can be determined. At 50 MeV/u the laboratory distributions were explicitly transformed event-by-event into the source frame determined from the above source velocity analysis using the Galilean transformation. For the 80 and 100 MeV/u reactions, the emission velocities were determined by the minor axes of the elliptical fits to the rapidity - perpendicular momentum distributions as they should be unaffected by the extended source velocity distribution.

The measured emission velocities, along with those from the $^{139}La + ^{12}C$ reaction at 18 MeV/u[25]), are shown in Figure 14 as a function of the fragment Z-value. At all energies the velocities decrease with increasing Z-value, as expected for Coulomb emission. This figure also shows that the emission velocity for a given Z-value decreases as the bombarding energy is increased. This can be explained by the charged particle loss either preceding or following the heavy fragment emission. Figures 1 and 2 show that the average coincidence charge decreases with increasing bombarding energy. If this charge is lost prior to scission, then the complex fragments would be emitted, on average, from systems that have a smaller total charge. Thus, the Coulomb repulsion energy and the corresponding emission velocity would be smaller. If the charge is emitted after scission, the observed secondary fragments would be emitted as heavier primary fragments, with smaller emission velocities.

Figure 15 shows the inclusive emission velocities for three bombarding energies, and the fragment velocities in the center-of-mass frame for 2-fold coincidence events in the 80 and 100 MeV/u reactions. To calculate the emission velocities from the coincidence events, a Lorentz transformation into the center-of-mass frame was applied. There is general agreement between the emission velocities calculated from the inclusive and the 2-fold coincidence events. The lines in Figure 15 are predictions of the emission velocity based upon the Viola fission fragment kinetic energy systematics[45]). Good agreement is observed for intermediate Z-values with the calculations deviating slightly from the data at low and high Z-values.

Since the Viola systematics have been compiled for symmetric fission, we have generalized it for asymmetric decay by solving for the radius parameter r_0 in equation (1):

$$E_{Viola} = \frac{1.44\ Z_1\ Z_2}{r_0\ (A_1^{1/3} + A_2^{1/3})}, \qquad (1)$$

with $Z_1 = Z_2$ and $A_1 = A_2$. The extracted r_0 was then used in (1) to calculate the kinetic energy released and the fragment velocities for asymmetric decay where $Z_1 \neq Z_2$ and $A_1 \neq A_2$.

To compare the predictions to the experimental data, corrections must be made for the loss of light charged particles. Since light particle emission can both precede or follow the main binary division, the emission velocities were calculated using two extreme assumptions. First, the assumption was made that the binary division preceded all of the light particle emission. The measured source velocity was used to infer the charge, mass and excitation energy of the composite system. The emission velocities after the binary decay were calculated from equation (1), and then evaporation corrections were performed for the hot primary fragments using the evaporation code PACE[46]). The dashed lines in Figure 15 are the emission velocities calculated assuming post-scission light charged particle emission.

In the above calculation, the excitation energy of the primary fragments was determined from the inferred excitation energy of the compound nucleus and the Q-values for the various binary divisions. The angular momenta (J_1) of the binary decay products were calculated in the sticking limit, $J_1 = (I_1/I_0)\ J_0$, from the spin distributions used in the statistical model calculations described below. Here J_1 and J_0 are the spin of the fragment and the compound nucleus, and I_1 and I_0 are the moments of inertia of the fragment and of the composite system. The moment of inertia of the composite system is $I_0 = I_1 + I_2 + \mu R^2$, where I_1 and I_2 are the moments of inertia of the fragment and its decay partner, μ is the reduced mass of the system, and R is the separation distance between the fragments at scission, which was taken to be $1.225\ (A_1^{1/3} + A_2^{1/3}) + 2$ fm.

The emission velocities were also calculated assuming that all of the light particle emission preceded the binary decay. A residue with the average charge measured from the $Z_1 + Z_2$ coincidence distributions was assumed to be formed following light particle emission. Statistical model calculations were performed to estimate the post-evaporative masses associated with the measured charges. The calculated masses were essentially the same as predicted by the $A = 2.08Z + 0.0029Z^2$ mass parameterization[21]). The extended Viola systematics was used as above to calculate the emission velocities of the binary decay products of the residual systems (solid line in Figure 15). The two predicted emission velocity distributions (solid and dashed lines) were found to be essentially identical over the Z-value range measured in the experiments. This indicates that the emission velocities are insensitive to small variations of the total mass of the system at scission.

Figure 16 shows emission velocity spectra for Z = 6 fragments from the reaction of 80 MeV/u $^{139}La + {}^{12}C$ at several angles in the source frame. These spectra were generated with an event-by-event Lorentz transformation of the inclusive data into the measured source frame. While the

yields are approximately a factor of 10 larger for backward emission than for forward emission, the shapes of the distributions are very similar. In contrast, for the same system at 18 MeV/u[25]) and for other lighter systems at 11 - 30 MeV/u[19,21-24]), the velocity distributions of the light fragments have high energy tails at backward angles. These tails indicate the incomplete relaxation of the entrance channel kinetic energy, and are evidence for the deep-inelastic production mechanism. At 80 MeV/u, however, the emission velocities for fragments near the target Z-value are completely relaxed at both forward and backward angles.

3.5 ANGULAR DISTRIBUTIONS

Statistical compound-nucleus emission requires the relaxation of the angular degrees of freedom prior to the decay process. The resulting fragment angular distributions are forward/backward symmetric. There are two limiting cases: the emission of light particles, such as neutrons and protons, which is nearly isotropic ($d\sigma/d\Omega \propto$ constant), and heavier fragment emission at high angular momentum, such as detected in this study, which is nearly isotropic in the reaction plane, thus $d\sigma/d\Omega = 1/\sin\theta$, or $d\sigma/d\theta$ = constant[15]).

For the 80 and 100 MeV/u reactions, the experimental data were transformed into a frame moving with the average source rapidity, as determined from the analysis described above. Angular distributions ($d\sigma/d\theta$) in this frame are presented in Figure 17 for representative Z-values. For fragments near symmetry (Z = 23), the distributions are nearly flat and consistent with statistical emission. However, for lighter and heavier Z-values, the distributions show sizable anisotropies. This restricted range of isotropic distributions is to be contrasted with the very broad range observed at lower bombarding energies[25]), where an isotropic component was observed for Z-values between the target and the projectile with an additional exponential component only for fragments near the target and projectile. With increasing bombarding energy, a smaller and smaller range of Z-values exhibits isotropic angular distributions.

Monte Carlo simulations were performed to investigate whether a range of isotropic sources could give rise to the observed anisotropic angular distributions. By assuming that the source mass depended upon the source velocity, anisotropic angular distributions can be generated. This is a reasonable assumption for an incomplete fusion mechanism. However, the resulting anisotropic angular distributions were still relatively independent of the fragment Z-value, in contrast to the observed evolution from backward to forward peaking in the data. Thus, these experimental angular distributions most probably originate from an intrinsically anisotropic emission process.

While the limited angular region spanned precludes the determination of complete angular distributions for the 50 MeV/u data, the ratio of the differential cross sections forward and backward of 90° in the source frame can be investigated at all bombarding energies. For the 50

MeV/u data, we define the forward/backward ratio as $\frac{\int d\sigma/d\theta\ (\theta < 90^\circ)}{\int d\sigma/d\theta\ (\theta > 90^\circ)}$ in the source frame. These ratios are shown in the bottom portion of Figure 18. The mean forward/backward ratio is 1.06±0.10 for Z-values in the range of 22-35, and is virtually independent of the fragment atomic number. Thus, these yields are symmetric about 90°, as required by the compound nucleus emission process.

For the larger bombarding energies, the forward/backward ratios are defined as above. However, in order to compensate for the difference in angular coverage as a function of Z-value, we have calculated the ratios from the fits to the angular distributions (see below) between 0° - 180°. In contrast to the 50 MeV/u reaction, at the larger bombarding energies the forward/backward ratios increase smoothly with increasing Z-value. The rate of change of the ratio with Z-value is slightly larger at 100 MeV/u than at 80 MeV/u. The anisotropy of the fragment angular distributions at 80 and 100 MeV/u strongly suggests that non-equilibrium processes account for much of the complex fragment yield.

3.6 CROSS SECTIONS

The differential cross sections at 50 MeV/u were integrated over 180° assuming a 1/sin θ angular distribution since the measured forward/backward ratios are consistent with equilibrium emission. The angle-integrated cross sections for the 80 and 100 MeV/u reactions were extracted from quadratic fits to the logarithm of the differential cross sections (solid lines in Figure 17). The angle-integrated cross sections for the $^{139}La + ^{12}C$ system at 18[25]), 50, 80 and 100 MeV/u are shown in Figure 19 as a function of fragment Z-value.

The charge distribution for fragments of $8 < Z < 40$ at 18 MeV/u[25]) is consistent with statistical emission from a system above the Businaro-Gallone transition point[47]). There is a maximum in the yield at symmetry (Z ~ 31) due to a minimum in the potential energy surface at this point. Between 18 and 50 MeV/u the charge distribution becomes flatter and the yields decrease. From 50 to 80 MeV/u the yields increase and the charge distribution becomes U-shaped. At 100 MeV/u the yields are larger still, however since fragments with $Z > 27$ were not observed, it is not clear whether the distribution is still U-shaped, or whether it has flattened out.

The observed flattening of the charge distribution between 18 and 50 MeV/u can be explained by the increase in temperature of the system, which tends to make all of the decay channels more equally probable. However, the decrease in the cross sections for symmetric products is somewhat puzzling. In the $^{93}Nb + ^{9}Be, ^{27}Al$ systems a similar decrease was attributed to the onset of the incomplete fusion process above ~ 20 MeV/u[22]).

The symmetric shape of the charge distribution at 80 MeV/u is another indication of the predominantly binary nature of the decay process. A large number of multibody events should give rise to monotonically decreasing charge distributions. Although this U-shape is incompatible with statistical emission from a system beyond the Businaro-Gallone point, it is not inconsistent with statistical emission from a system that has lost a large amount of charge, or angular momentum, or both, prior to the emission process. Thus, we can draw no conclusions about the equilibrium or non-equilibrium nature of the process solely from the shape of the charge distributions.

3.7 CHARGE LOSS DISTRIBUTIONS

In Figure 2, the peak in the distribution of total detected charge for the 2-fold coincidence events shifts to smaller values and the width increases as the bombarding energy increases. Is the missing charge due to undetected light complex fragments, or rather, due to an increase in the multiplicity of evaporated protons and alpha particles? By examining the total charge distributions as a function of the complex fragment multiplicity, one may shed some light on this question. Figure 20 shows that the total charge distributions are insensitive to the complex fragment multiplicity at both 80 and 100 MeV/u. This lack of a dependence indicates that the two-fold and higher-order complex fragment events arise from a common source and suggests that all of the missing charge is in the form of undetected light particles.

Similarly, the rapidity of the center-of-mass also shows no dependence on the multiplicity of complex fragments (Figure 11). These two results are strong evidence for the common origin of all of the complex fragments. The 3- and 4-fold coincidences do not seem to pick out a special class of events with substantially larger momentum transfer or excitation energy, in contrast to results at lower bombarding energy[39,44]).

The average charge loss for coincidence events ($<\Delta Z>$) is shown as a function of the center-of-mass energy for the $^{139}La + ^{12}C$ system in Figure 21. The slope of the solid line is about 50 MeV per charge unit. This value is close to that observed experimentally in the 18 MeV/u $^{139}La + ^{64}Ni$ system[44]), and is also in reasonable agreement with the statistical emission calculations shown in Fig. 22. The solid line in Figure 21 does not pass through zero, presumably because only neutrons are emitted from the neutron-rich primary fragments at low excitation energy.

The average charge loss for two-fold coincidence events is presented in Figure 22 as a function of the Z-value of one of the fragments. While the charge loss increases with increasing bombarding energy for all mass asymmetries, the shapes of these three distributions are similar. The charge loss distributions go through minima near symmetry, rise again for heavier fragments, before finally decreasing for the heaviest detected fragments at 80 and 100 MeV/u.

Between 50 - 100 MeV/u the measured source/beam rapidity ratio is, within error bars, independent of bombarding energy, and corresponds to a composite system with an atomic number of ~ 60. Corrections for light charged particle evaporation, assuming post-scission emission, have been performed with the evaporation code PACE[46]) as described above. The prediction of the charge loss distribution from the PACE simulations is shown by the dashed lines in Figure 22. The solid lines show statistical model calculations (described below) that include both light charged particle emission and complex fragment emission. Both models underpredict the measured charge loss somewhat, although the PACE simulations do a slightly better job at the larger bombarding energies.

Although in absolute magnitude the data and the model predictions differ slightly, their shapes are similar. Light complex fragments tend to evaporate more charged particles per unit excitation energy than do heavier fragments, due to the smaller Coulomb barriers for charged particle emission. Both the experimental distributions and the statistical calculations pass through minima for symmetric decay, in which no light complex fragments are emitted, and then rise again for the larger fragments, which are emitted in coincidence with a light complex fragment. Hence, it appears that the potential energy surface influences the light charged particle emission process to some degree.

4. Model Calculations and Discussion

The complex fragment component observed in the $^{139}La + ^{12}C$ reaction at 14 and 18 MeV/u has been explained by complete fusion followed by the sequential compound-nucleus statistical decay of the equilibrated fusion product[25]). In the following subsections, the experimental results from the 50, 80 and 100 MeV/u $^{139}La + ^{12}C$ reactions are compared to the incompletefusion compound-nucleus statistical-emission model, which has successfully explained the results of asymmetric reactions at bombarding energies of 25 & 30 MeV/u[19,21]).

4.1. INCOMPLETE FUSION

The source rapidities, as determined from both inclusive and coincidence events, indicate that for bombarding energies between 50 and 100 MeV/u, complete fusion has given way to incomplete fusion, in agreement with many previous studies[26-30]). A simple prescription to estimate the mass transfer, momentum transfer, and excitation energy of the incomplete fusion product from the measured source rapidity is to assume that all of the beam momentum is given to the incomplete fusion product and that the lighter reaction partner is sheared in the incomplete fusion process.

Using this prescription we have[43]):

$$A_{Trans} = \frac{P_{beam}c}{uc^2 \sinh(Y)} - A_P, \qquad (2)$$

where A_p is the projectile mass, P_{beam} is the beam momentum, Y is the experimentally determined source rapidity, u is the energy equivalent of one atomic mass unit (931.5 MeV/c^2), and A_{Trans} is the calculated mass transferred from the ^{12}C target to the ^{139}La projectile.

From the mass transferred to the projectile, the deposited excitation energy can be calculated as[43]):

$$E^* = E_{beam} - E_{IF} + Q = E_{beam} - uc^2 \cosh(Y) (A_P + A_{Trans}) + Q . \qquad (3)$$

Here E_{beam} is the beam energy, E_{IF} is the kinetic energy of the incomplete fusion product, and Q is the ground state Q-value of the incomplete fusion process. The Q-values for the incomplete fusion reactions were calculated to be approximately -20 MeV, assuming two fragments in the exit channel (incomplete-fusion product and the target remnant). The Q-values could range as low as -45 MeV if, instead, the non-fusing portion of the ^{12}C target escapes as single nucleons. However, the Q-value is a small fraction of the total excitation energy in these reactions.

The calculated mass transfers, excitation energies, and momentum transfers in the projectile frame ("normal kinematics") are shown in Table 1. A geometrical - kinematical incomplete fusion model[32]) predicts similar values for the mass transfers, momentum transfers, and excitation energies.

4.2 STATISTICAL DECAY CALCULATIONS

The statistical decay calculations were performed using the Monte Carlo code GEMINI[22]). In this code the decay widths for the emission of heavy fragments (Z > 2) are calculated using the transition state formalism[16,17]), and the decay widths for the emission of light particles (Z ≤ 2) are calculated using the Hauser-Feshbach formalism[48]). Details of this calculation, including expressions for the transmission coefficients and the strong absorption radii are described in reference 22. In these calculations, the nuclear level density parameter "a" was taken to be a = A_{CN} / 8.5 MeV^{-1}. The saddle point energies, as a function of mass asymmetry and angular momentum, were calculated by Carjan and Alexander[49]) using the Rotating Finite Range Model (Yukawa-plus-exponential potential, plus a surface diffuseness term)[50]).

At each decay step, all possible binary decays, from neutron and proton evaporation through symmetric fission, were considered. After each decay, the heavy (Z > 2) secondary fragments were allowed to decay again until all the excitation energy was exhausted. Following the emission

of a heavy fragment, the remaining excitation energy was apportioned assuming equal temperatures in the two fragments. The angular momentum partition was calculated in the sticking limit. Thermal fluctuations in both the excitation energy division[51]) and in the angular momentum partition[52,53]) were incorporated.

Calculating the charge distributions requires the summation of the entrance channel ℓ-waves as:

$$\sigma(Z) = \pi\lambda\!\!\!^{-2} \sum_{\ell=0}^{\ell=\ell_{max}} (2\ell+1)\, T_\ell(Z), \qquad (4)$$

where $T_\ell(Z)$ are the probabilities of the given decays proceeding at angular momentum ℓ.

At low energy (< 20 MeV/u) where complete fusion reactions dominate, the statistical model calculations have been summed to the ℓ_{max} that provides the best fit to the experimental data. The shapes of the calculated and measured $\sigma(Z)$ distributions can be compared, as well as the values of ℓ_{max} used in the calculation and predicted by fusion models[54-57]). Good agreement with the shapes of the experimental cross section has been obtained using values of ℓ_{max} predicted by the fusion models[22,25]).

At larger bombarding energies incomplete fusion sets in. There are two problems associated with applying the statistical emission theory to incomplete fusion reactions. First, it is not apparent that the triangular ℓ-wave distribution used for complete fusion reactions represents the spin distribution of the incomplete fusion products. Second, the theoretical cross sections are very dependent upon the choice of ℓ_{max}, and there are no reliable models from which this quantity can be determined.

The simplest assumption is to retain the triangular shape of the spin distribution. One then assumes that for every entrance channel ℓ-wave the fractional angular momentum transfer is equal to the fractional linear momentum transfer. For incomplete fusion Eq. (4) is replaced by:

$$\sigma(Z) = \pi\lambda\!\!\!^{-2} \sum_{\ell=0}^{\ell=J_{max}/f_P} (2\ell+1)\, T_\ell(Z), \qquad (5)$$

with $J = f_P \ell$, where J is the spin transferred to the incomplete fusion product, and f_P is the fractional linear momentum transfer.

At lower bombarding energy it was necessary to subtract an exponential component from the total yield to obtain the isotropic cross sections for Z-values near the target[19,21-23,25]). A similar procedure was attempted for the 80 and 100 MeV/u data for those Z-values with anisotropic angular distributions. While it was shown above that the differential cross sections of these products do not consist of flat components plus exponential components as they do at lower energy

(see Figure 17), the compound statistical model allows for different shapes of the angular distributions depending upon the angular momentum, the moment of inertia, and the temperature of the nucleus.

In the statistical model, the quantity $\frac{J^2}{2I_{eff}\,T}$ determines the angular distributions of the decay products[17,58]). Here J is the nuclear spin, T the nuclear temperature, and I_{eff} is the effective moment of inertia of the conditional saddle point, $I_{eff} = \frac{1}{I_{eff}} = \frac{1}{I_{||}} - \frac{1}{I_{\perp}}$, where $I_{||}$ and $I_{\perp}$ are, respectively, the moments of inertia parallel and perpendicular to the nuclear symmetry axis. When the above quantity is large, the $d\sigma/d\theta$ angular distributions are independent of θ. On the other hand, when the quantity is small, the angular distributions are proportional to sin θ. Angular distributions intermediate between these two extremes are possible as long as they are symmetric about 90° in the frame of the compound nucleus. To allow for these different angular distributions, the experimental cross sections have been decomposed into components forward and backward of 90°. The smaller of these two components (the component forward of 90° for the lighter fragments and backward of 90° for the heavier fragments) was assumed to result entirely from statistical emission. The "absolute" statistical cross sections were then determined by multiplying the smaller component by two. These cross section are shown as the open points in Figure 23.

The cross sections for the fragments with isotropic angular distributions (solid points) have been used to determine the J_{max} of the GEMINI calculations. Table 1 gives the excitation energies and the fractional linear momentum extracted from the experimental source rapidity, and the J_{max} of the triangular distributions that were used in the statistical model calculations for the systems studied in this work. For these incomplete fusion reactions, J_{max} should be regarded as no more than a fitting parameter, however the values are quite similar to experimental and theoretical values of ℓ_{max} determined from complete fusion reactions in the same system at lower bombarding energy[25]).

The uncertainties in the input parameters of the statistical code, specifically in the angular momentum distribution, do not allow for quantitative comparisons with the experimental data. However, the qualitative agreement with the experimental data is very good at 50 MeV/u. The shape of the distribution and the absolute magnitude of the cross sections can be explained using reasonable assumptions about the excitation energy and angular momentum distribution. This is strong evidence for the compound-nucleus statistical nature of the process. There are no inexplicably large cross sections due to non-equilibrium processes or due to the onset of another reaction mechanism.

As at 50 MeV/u, it is possible to reproduce the symmetric cross sections at both 80 and 100 MeV/u with reasonable assumptions about the excitation energy and angular momentum of the

equilibrated system (see Table 1). From the J_{max} values used to fit the complex fragment cross sections near symmetry the total compound nucleus cross sections can be inferred (see Table 1). While the cross sections for statistical emission of complex fragments rise with increasing bombarding energy (as do the total complex fragment cross sections), the inferred total compound nucleus cross sections decrease.

The histograms in Figure 23 show the results of statistical decay calculations for ^{146}Nd. At 80 and 100 MeV/u the calculated distributions are flatter than the experimental distributions. The underprediction of the statistical cross sections for Z-values ≤ 15 in Figure 23 may indicate that the non-equilibrium component extends forward of 90° for these fragments (see below). The slight overprediction of the cross sections for the largest Z-values may be a systematic error related to extrapolations of the limited angular distributions for these fragments (see Figure 17).

The measured (points) and calculated (histograms) $d\sigma/d\theta$ angular distributions in the source frame are shown in Figure 24 for several Z-values from the 80 and 100 MeV/u ^{139}La + ^{12}C reactions. For all Z-values the calculated angular distributions are flat (within statistical errors) within the angular region of approximately 20° - 160°, and fall off rather steeply at smaller and larger angles. These calculated angular distributions are similar to those measured in low-energy heavy-ion induced fission reactions[59]). Hence, the side-peaking observed in the experimental distributions of the lightest fragments can not be explained as a temperature effect (a decrease in the ratio $\frac{J^2}{2I_{eff}\,T}$ as described above), but rather seems to be due to non-equilibrium effects. This is clearly illustrated by comparing the measured and calculated differential cross sections for the smallest Z-values. Even at angles smaller than 90°, the measured differential cross sections are significantly larger than the calculated values. This suggests that the non-equilibrium light fragments, which were confined to very backward angles in reverse kinematic reactions at lower bombarding energy[25]), extend forward of 90° at 80 and 100 MeV/u.

4.3 THE ANISOTROPIC COMPONENT

It is interesting to speculate about the nature of the anisotropic yield and whether it might be due to the transition from the incomplete fusion regime to the fireball regime.

In the fireball model[33-35]), the nuclear matter is divided into three regions - the projectile spectator, the target spectator, and the fireball, in which the nucleons in the target and spectator overlap. In an instantaneous projectile-target interaction, the thermal energy per nucleon in the fireball is much larger than the nucleon binding energy. Thus, it is likely that the participants in the fireball region would be emitted entirely as nucleons. The complex fragments that are observed in asymmetric reactions at E/A >> 100 MeV/u are emitted very nearly isotropically[60-62]). These

products have been explained as resulting from the decay of the excited target spectator in a two-step reaction mechanism[63])

When the relative velocity is not large enough for the fireball to decouple quickly from the spectator fragments, the system may partially equilibrate before separating. In the limit of complete equilibration, we have the incomplete and complete fusion processes seen at lower energy.

At a critical bombarding energy, which will depend upon the target-projectile combination, one should observe a transition from the incomplete fusion mechanism to the fireball mechanism. This transition may not be particularly sharp as it will also depend upon impact parameter. A geometrical-kinematic model that gives some insight into this process is described in reference[32]). Just below the threshold bombarding energy, when the proto-fireball is captured by the projectile-spectator, the product nuclear system may have an elongated shape. If this nuclear system subsequently decays before the shape degree of freedom is able to relax, the emitted complex fragment should point towards the light spectator and its angular distributions could be influenced by the dynamical interaction process. Similarly, just above the threshold bombarding energy, the fireball and the target spectator will have a relative velocity determined mainly by their mutual Coulomb repulsion. In either of these scenarios, the rather long interaction time between the fireball and the spectator fragment could allow for a large amount of energy thermalization and mass transfer, and could give rise to the observed anisotropic complex fragments.

5. Summary and Conclusions

The incomplete-fusion compound-nucleus statistical-decay model has successfully described the results of asymmetric reactions at bombarding energies $\leq$ 30 MeV/u[19,21-23,25]). For the 50 MeV/u ^{139}La + ^{12}C reaction, we have shown that following incomplete fusion, the complex fragments are produced in highly equilibrated binary processes. Incomplete fusion is indicated by the source rapidity distribution, which is very sharp and corresponds to the ^{139}La projectile capturing approximately one-half of the ^{12}C target. The experimental source rapidities are independent of Z-value within the range of $21 \leq Z \leq 35$, showing the common origin of all of the complex fragments.

The binary nature of the decay process is illustrated by the 2-fold coincidence events (Z_1 + Z_2), which sum to a nearly constant total charge, by the Z versus velocity contour plots, which show Coulomb ridges characteristic of relaxed binary decay, and by the well-defined Coulomb rings in the $\frac{\partial^2\sigma}{\partial v_{\|}\partial v_{\perp}}$ density plots.

The relaxed nature of the decay process is shown by the source frame emission velocities and angular distributions. The fragment emission velocities show excellent agreement with the

predictions of completely relaxed (Coulomb) binary decay. The forward/backward symmetry of all of the fragment angular distributions demonstrates the complete relaxation of the angular degrees of freedom.

We have used the average experimental source rapidity to infer the mass, charge, excitation energy, and angular momentum distribution of the incomplete fusion product. To determine conclusively whether the complex fragments are produced by compound nucleus decay, it is necessary to compare the absolute cross sections with predictions from the compound-nuclear statistical-decay model[16,17]). A statistical decay code, GEMINI[22]), based on this model, which has had great success in reproducing the complex fragment cross sections following complete fusion reactions at lower bombarding energies[22,23,25]), is also able to reproduce the experimental cross sections in this reaction. The excellent agreement between the statistical model calculations and the experimental data in the $^{139}La + ^{12}C$ system from 14 - 50 MeV/u is very strong evidence for compound nucleus formation in this energy range.

For the higher energy 80 and 100 MeV/u $^{139}La + ^{12}C$ reactions, we also have evidence for highly equilibrated binary decay processes following incomplete fusion. The source rapidities correspond to incomplete fusion processes in which approximately one-half of the ^{12}C target is transferred to the ^{139}La projectile. The source rapidity distributions are independent of Z-value and of the complex fragment multiplicity, showing the common origin of all of the complex fragments.

The binary nature of the process is illustrated by the peaks in the $(Z_1 + Z_2)$ charge distributions, by the Coulomb ridges in the Z versus velocity contour plots, by the well-defined elliptical distributions in the rapidity-perpendicular momentum plots, and by the symmetric charge distribution at 80 MeV/u. The fragment emission velocities are Coulombic and completely relaxed. However, except for the fragments from symmetric and nearly symmetric decay (Z ~ 20-24), the source frame angular distributions are anisotropic and inconsistent with purely statistical emission. Similarly, while a limited range of Z-values near symmetry can be explained as originating solely from compound-nucleus statistical decay following incomplete fusion, the yield for asymmetric decay is far larger than predicted by this model.

*This work was supported by the Director, Office of Energy Research, Division of Nuclear Physics of the Office of High Energy and Nuclear Physics of the U.S. Department of Energy under Contract DE-AC03-76SF00098.

[1]Present address: National Superconducting Cyclotron Laboratroy, Michigan State University, E. Lansing, MI 48824

[2]Present address: Washington University, St. Louis, MO 63130

[3]Present address: Institute of Atomic Energy, Beijing, China

[4]Present address: Massachusetts Institute of Technology, Cambridge, MA 02139

References

1) W.G. Lynch, Ann. Rev. Nucl. Sci. **37** (1987) 493, and references contained therein.

2) L. G. Moretto and G. J. Wozniak, Prog. in Part. & Nucl. Phys. **21** (1988) 401, and references contained therein.

3) U. Lynen, H. Ho, W. Kuhn, D. Pelte, U. Winkler, W.F.J. Mueller, Y.-T. Chu, P. Doll, A. Gobbi, K. Hildenbrand, A. Olmi, H. Sann, H. Stelzer, R. Bock, H. Lohner, R. Glasow, and R. Santo, Nucl. Phys. **A387** (1982) 129c

4) C.B. Chitwood, D.J. Fields, C.K. Gelbke, W.G. Lynch, A.D. Panagiotou, M.B. Tsang, H. Utsunomiya, and W.A. Friedman, Phys. Lett. **B131** (1983) 289

5) B.V. Jacak, G.D. Westfall, C.K. Gelbke, L.H. Harwood, W.G. Lynch, D.K. Scott, H. Stocker, M.B. Tsang, and T.J.M. Symons, Phys. Rev. Lett. **51** (1983) 1846

6) L.G. Sobotka, M.L. Padgett, G.J. Wozniak, G. Guarino, A.J. Pacheco, L.G. Moretto, Y. Chan, R.G. Stokstad, I. Tserruya, and S. Wald, Phys. Rev. Lett. **51** (1983) 2187

7) D.J. Fields, W.G. Lynch, C.B. Chitwood, C.K. Gelbke, M.B. Tsang, H. Utsunomiya, and J. Aichelin, Phys. Rev. **C30** (1984) 1912

8) D.E. Fields, K. Kwiatkowski, D. Bonser, R.W. Viola, V.E. Viola, W.G. Lynch, J. Pochodzalla, M.B. Tsang, C.K. Gelbke, D.J. Fields, and Sam Austin, Phys. Lett. **B220** (1989) 356.

9) B. Borderie, M. Montoya, M.F. Rivet, D. Jouan, C. Cabot, H. Fuchs, D. Gardes, H. Gauvin, D. Jacquet, and F. Monnet, Phys. Lett. **B205** (1988) 26

10) M.W. Curtin, H. Toki, and D.K. Scott, Phys. Lett. **B123** (1983) 289.

11) J. Aichelin and J. Huefner, Phys. Lett. **B136** (1984) 15.

12) B.V. Jacak, D. Fox, and G.D. Westfall, Phys. Rev. **C31** (1985) 704.

13) L.G. Sobotka, M.A. McMahan, R.J. McDonald, C. Signarbieux, G.J. Wozniak, M.L. Padgett, J.H. Gu, Z.H. Liu, Z.Q. Yao, and L.G. Moretto, Phys. Rev. Lett. **53** (1984) 2004

14) M.A. McMahan, L.G. Moretto, M.L. Padgett, G.J. Wozniak, L.G. Sobotka, and M.G. Mustafa, Phys. Rev. Lett. **54** (1985) 1995

15) Robert Vandenbosch and John R. Huizenga, Nuclear Fission, (Academic Press, New York, 1973)

16) L.G. Moretto, Phys. Lett. **B40** (1972) 185

17) L.G. Moretto, Nucl. Phys **A247** (1975) 211

18) G. Auger, D. Jouan, E. Plagnol, F. Pougheon, F. Naulin, H. Doubre, and C. Gregoire, Z. fur Phys. **A321** (1985) 243

19) R.J. Charity, M.A. McMahan, D.R. Bowman, Z.H. Liu, R.J. McDonald, G.J. Wozniak, L.G. Moretto, S. Bradley, W.L. Kehoe, A.C. Mignerey, and M.N. Namboodiri, Phys. Rev. Lett. **56** (1986) 1354

20) F. Auger, B. Berthier, A. Cunsolo, A. Foti, W. Mittig, J.M. Pascaud, E. Plagnol, J. Quebert, and J.P. Wieleczko, Phys. Rev. **C35** (1987) 190

21) R.J. Charity, D.R. Bowman, Z.H. Liu, R.J. McDonald, M.A. McMahan, G.J. Wozniak, L.G. Moretto, S. Bradley, W.L. Kehoe, and A.C. Mignerey, Nucl. Phys. **A476** (1988) 516

22) R.J. Charity, M.A. McMahan, G.J. Wozniak, R.J. McDonald, L.G.Moretto, D.G. Sarantities, L.G. Sobotka, G. Guarino, A. Pantaleo, L. Fiore, A. Gobbi, and K.D. Hildenbrand, Nucl. Phys. **A483** (1988) 371

23) H.Y. Han, K.X. Jing, E. Plagnol, D.R. Bowman, R.J. Charity, L. Vinet, G.J. Wozniak, and L.G. Moretto, Nucl. Phys. **A492** (1989) 138

24) E. Plagnol, L. Vinet, D.R. Bowman, Y.D. Chan, R.J. Charity, E. Chavez, S.B. Gazes, H. Han, W.L. Kehoe, M.A. McMahan, L.G. Moretto, R.G. Stokstad, G.J. Wozniak, and G. Auger, Phys. Lett. **B221** (1989) 11

25) R.J. Charity, K. Jing, D.R. Bowman, M.A. McMahan, G.J. Wozniak, L.G. Moretto, N. Colonna, G. Guarino, A. Panteleo, L. Fiore, A. Gobbi, and K. Hildenbrand, Nucl. Phys. **A511** (1990) 59

26) V.E. Viola, Jr., B.B. Back, K.L. Wolf, T.C. Awes, C.K. Gelbke, and H. Breuer, Phys. Rev. **C26** (1982) 178

27) J. Galin, H. Oeschler, S. Song, B. Borderie, M.F. Rivet, I. Forest, R. Bimbot, D. Gardes, B. Gatty, H. Guillemot, M. Lefort, B. Tamain, and X. Tarrago, Phys. Rev. Lett. **48** (1982) 1787

28) Y. Chan, M. Murphy, R.G. Stokstad, I. Tserruya, S. Wald, and A. Budzanowski, Phys. Rev. **C27** (1983) 447

29) H. Morgenstern, W. Bohne, W. Galster, K. Grabisch, and A. Kyanowski, Phys. Rev. Lett. **52** (1984) 1104

30) G.S.F. Stephans, D.G. Kovar, R.V.F. Janssens, G. Rosner, H. Ikezoe, B. Wilkins, D. Henderson, K.T. Lesko, J.J. Kolata, C.K. Gelbke, B.V. Jacak, Z.M. Koenig, G.D. Westfall, A. Szanto de Toledo, E.M. Szanto, and P.L. Gonthier, Phys. Lett. **B161** (1985) 60

31) G. Auger, E. Plagnol, D. Jouan, C. Guet, D. Heuer, M Maurel, H. Nifenecker, C. Ristori, F. Schussler, H. Doubre, and C. Gregoire, Phys. Lett. **B169** (1986) 161

32) L.G. Moretto and D.R. Bowman, Proceedings of the XXIV International Winter Meeting on Nuclear Physics, Bormio, Italy, ed. I. Iori, Ricerca Scientifica ed Educazione Permanente, Suppl. **49** (1986) 126

33) J.D. Bowman, W.J. Swiatecki, and C.F. Tsang, Lawrence Berkeley Laboratory Report LBL - 2908 (1973)

34) G.D. Westfall, J. Gosset, P.J. Johansen, A.M. Poskanzer, W.G. Meyer, H.H. Gutbrod, A. Sandoval, and R. Stock, Phys. Rev. Lett. **37** (1976) 1202

35) J. Gosset, H.H. Gutbrod, W.G. Meyer, A.M. Poskanzer, A. Sandoval, R. Stock, and G.D. Westfall, Phys. Rev. **C16** (1977) 629

36) G.F. Bertsch and P.J. Siemens, Phys. Lett. **B126** (1983) 9

37) S. Harar, Nucl. Phys. **A471** (1987) 205c

38) R. Trockel, K.D. Hildenbrand, U. Lynen, W.F.J. Muller, H.J. Rabe, H. Sann, H. Stelzer, W. Trautmann, R. Wada, E. Eckert, P. Kreutz, A. Kuhmichel, and J. Pochodzalla, Phys. Rev. **C 39** (1988) 729

39) Y. Blumenfeld, N. Colonna, D.N. Delis, K. Hanold, J.C. Meng, G.F. Peaslee, G.J. Wozniak, L.G. Moretto, B. Libby, G. Guarino, N. Santoruvo, and I. Iori, Lawrence Berkeley Laboratory Preprint LBL-28472, and submitted to Phys. Rev. Lett. (1990)

40) D.R. Bowman, W.L. Kehoe, R.J. Charity, M.A. McMahan, A. Moroni, A. Bracco, S. Bradley, I. Iori, R.J. McDonald, A.C. Mignerey, L.G. Moretto, M.N. Namboodiri, and G.J. Wozniak, Phys. Lett. **B189** (1987) 282

41) J.B. Moulton, J.E. Stephenson, R.P. Schmitt, and G.J. Wozniak, Nucl. Instr. Meth. **157** (1978) 325

42) J.T. Walton, H.A. Sommer, G.J. Wozniak, G.F. Peaslee, D.R. Bowman, W.L. Kehoe, and A. Moroni, Lawrence Berkeley Laboratory Report, LBL-27949.

43) D.R. Bowman, Ph.D. Thesis, Lawrence Berkeley Laboratory Report LBL-27691 (1989)

44) N. Colonna, R.J. Charity, D.R. Bowman, M.A. McMahan, G.J. Wozniak, L.G. Moretto, G. Guarino, A. Panteleo, L. Fiore, A. Gobbi, and K.D. Hildenbrand, Phys. Rev. Lett. **62** (1989) 1833

45) V.E. Viola, K. Kwiatkowski, and M. Walker, Phys. Rev. **C31** (1985) 1550

46) A. Gavron, Phys. Rev. **C21** (1980) 230

47) U.L. Businaro and S. Gallone, Nuovo Cim. **1** (1955) 629, 1277

48) H. Hauser and H. Feshbach, Phys. Rev. **87** (1952) 366

49) N. Carjan and J.M. Alexander, Phys. Rev. **C38** (1988) 1692

50) Arnold J. Sierk, Phys. Rev. **C33** (1986) 2039

51) D.J. Morrissey and L.G. Moretto, Phys. Rev. **C23** (1981) 1835

52) L.G. Moretto and R.P. Schmitt, Phys. Rev. **C21** (1980) 204

53) R.P. Schmitt and A.J. Pacheco, Nucl. Phys. **A379** (1982) 313

54) R. Bass, Nucl. Phys. **A231** (1974) 45

55) R. Bass, Phys. Rev. Lett. **39** (1977) 265

56) W.J. Swiatecki, Nucl. Phys. **A376** (1982) 275 (1982).

57) S. Bjornholm and W.J. Swiatecki, Nucl. Phys. **A391** (1982) 471

58) I. Halpern and V.M. Strutinsky, Proc. 2nd U.N. Int. Conf. Peaceful Uses At. Energy, **15** (1958) 408.

59) G. E. Gordon, A. E. Larsh, T. Sikkeland, and G. T. Seaborg, Phys. Rev. **120** (1960) 1341.

60) A.I. Warwick, H.H. Wieman, H.H. Gutbrod, M.R. Maier, J. Peter, H.G. Ritter, H. Stelzer, F. Weik, M. Freedman, D.J. Henderson, S.B. Kaufman, E.P. Steinberg, and B.D. Wilkins, Phys.Rev. **C27** (1983) 1083

61) D.R. Bowman, R.J. Charity, H. Han, K. Jing, M.A. McMahan, R.J. McDonald, L.G. Moretto, G.J. Wozniak, W.L. Kehoe, B. Libby, and A.C. Mignerey, Proceedings of the 8th High Energy Heavy Ion Study, LBL - 24580 (1987) 352

62) S. Yennello, K. Kwiatkowski, D.E. Fields, R. Planeta, V.E. Viola, Y. Cassagnou, R. Dayras, S. Harar, R. Legrain, E.C. Pollacco, C. Volant, and E. Hourani, Indiana University Nuclear Chemistry Report, INC-40007-55 (1988) 31

63) A.M. Poskanzer, G. W. Butler, and E. K. Hyde, Phys. Rev. **C3** (1971) 882

Table 1. The momentum transfer, mass transfer, excitation energy and angular momentum of the equilibrated system formed in the $^{139}La + ^{12}C$ reactions at three bombarding energies.

E/A	Y/Y_{beam}	"P_{TR}"	mass	E* (MeV)	J_{max} ($\hbar$)	σ_{CN} (barns)
50	.96±.01	.52±.13	145.6±1.6	280±70	55	1.21
80	.95±.01	.57±.09	146.4±1.1	500±70	55	0.62
100	.95±.01	.57±.09	146.5±1.1	625±90	58	0.55

Figure Captions

Fig. 1. Linear contour plots of 2-fold Z_2 versus Z_1 coincidence events from the 18[25]), 50, 80, and 100 MeV/u $^{139}La + ^{12}C$ reactions. The sets of four lines correspond to contours with relative ratios of 4:3:2:1. The dashed lines indicate the total charge (63) of the projectile and target. At 18 MeV/u, the distributions spread above this line due to the imperfect Z-resolution of the detectors and to the smoothing of the contour map. The distributions from the 80 and 100 MeV/u reactions have been reflected about the line $Z_1 = Z_2$ to remove the bias due to the asymmetric detector configuration.

Fig. 2. Distributions of the total detected charge ($Z_1 + Z_2$) for 2-fold coincidence events from the 18[25]), 50, 80, and 100 MeV/u $^{139}La + ^{12}C$ reactions. The arrows indicate the sum of the projectile and target charge (63). The centroid and (width) of each distributions is indicated.

Fig. 3. Linear contours of the inclusive Galilean-invariant cross section $\frac{\partial^2\sigma}{v^2\partial\Omega\partial v}$ in the Z - velocity plane for the 50 MeV/u $^{139}La + ^{12}C$ reaction. There are a total of 37 contours with relative ratios of 1 to 37. The limits of the detector acceptance were 3^o to 8^o in the lab. The dashed curve is the experimental threshold for particles which punch through the telescopes.

Fig 4. Logarithmic contours of the inclusive Lorentz-invariant cross section $\frac{\partial^2\sigma}{\gamma^4 v^2\partial\Omega\partial v}$ in the Z - velocity plane from the 80 MeV/u $^{139}La + ^{12}C$ reaction at laboratory angles of 2.5^o, 4.5^o, 6.5, and 8.5^o. Neighboring contours differ in value by approximately a factor of 5 at 2.5^o, a factor of 4 at 4.5^o, a factor of 3 at 6.5^o, and a factor of 3 at 8.5^o.

Fig. 5. Same as Fig. 4 for the 100 MeV/u $^{139}La + ^{12}C$ reaction.

Fig. 6. (a) Schematic representation in the $v_{\|}$ - $v_{\perp}$ plane of complex fragment emission from a well-defined source (compound nucleus) with velocity, V_S. The Coulomb rings, upon which the fragments are emitted, are smeared out by light particle emission and by thermal fluctuations of the Coulomb energy[17]). The geometric limits of detector acceptance are shown by the dashed lines. The solid area is the predicted experimental distribution. (b,c,d) Experimental distributions of $\frac{\partial^2\sigma}{\partial v_{\|}\partial v_{\perp}}$ for the indicated Z bins from the 50 MeV/u $^{139}La + ^{12}C$ reaction. The size of the points indicates the density of the distribution. Arrows 1, 2, and 3 denote the beam velocity, the extracted source velocity, and the velocity for complete fusion, respectively.

Fig. 7. Experimental distributions of $\frac{\partial^2\sigma}{\partial Y\, \partial(P_\perp/mc)}$ for representative Z-values between 6 and 38 from the 80 MeV/u $^{139}La + ^{12}C$ reaction. The upper arrows in each subplot correspond to the beam rapidity and the lower arrows to the rapidity of the center-of-mass. Red indicates the regions of highest intensity.

Fig. 8. Same as Fig. 7 for the 100 MeV/u $^{139}La + ^{12}C$ reaction.

Fig. 9. Ratios of the source rapidity to the beam rapidity extracted from the inclusive events (open circles) and the 2-fold coincidence events (solid circles), as a function of Z-value, from the 50, 80, and 100 MeV/u $^{139}La + ^{12}C$ reactions. The bars on each point from the 50 MeV/u reaction are the statistical errors; at the higher energies the statistical errors are typically smaller than the data points. The solid lines show the mean source rapidities extracted from the inclusive data. The large error bars indicate the possible systematic errors associated with the energy calibrations and mass parameterizations. The dashed lines are the rapidities corresponding to complete fusion.

Fig. 10. The emission velocity as a function of emission angle for Z = 26 fragments from the 80 MeV/u $^{139}La + ^{12}C$ reaction. The solid points show the experimental data and error bars. The dashed line is a fit of the data points to an elliptical distribution as discussed in the text. The solid line is the prediction of a Monte Carlo program that assumes emission with a well-defined velocity from a range of sources with the measured source rapidity distribution (see Figure 11).

Fig. 11. Distributions of the center-of-mass rapidity for 2-fold, 3-fold, and 4-fold complex fragment (Z > 2) events from the 80 and 100 MeV/u $^{139}La + ^{12}C$ reactions. The arrows at the larger value of rapidity in each subplot indicate the beam rapidity. The arrows at the smaller value of rapidity indicate the center-of-mass rapidity of the entrance channel.

Fig. 12. The widths of the source rapidity and source momentum distributions along the x and y axes (P_x and P_y) as a function of the center-of-mass energy for $^{139}La + ^{12}C$ reaction. The statistical errors are smaller than the data points. The lines are linear fits to the data points.

Fig. 13. The average ratio of the source rapidity to the beam rapidity from the $^{139}La + ^{12}C$ reaction as a function of bombarding energy. The two lowest energy data points are taken from reference 25. These ratios were determined from inclusive (open circles) and 2-fold (solid circles) complex fragment events. All of the statistical errors are smaller than the data points. The bars on the inclusive points indicate the possible systematic errors from the energy calibrations and mass

parameterizations. The solid line corresponds to the experimental momentum transfer systematics [26-30].

Fig. 14. Fragment emission velocities, as a function of Z-value, extracted from the inclusive data in the 18[25]), 50, 80, and 100 MeV/u $^{139}La + ^{12}C$ reactions. In all cases the statistical errors are smaller than the data points.

Fig. 15. Fragment emission velocities, as a function of Z-value, from inclusive (open circles) and 2-fold coincidence (solid circles) events from the 50, 80, and 100 MeV/u $^{139}La + ^{12}C$ reactions. In all cases the statistical errors are smaller than the data points. The lines are predictions of the expected emission velocities from the Viola fission fragment kinetic energy systematics[45]), which was generalized to include decays at all charge asymmetries. The dashed line shows the predicted emission velocities assuming that the binary decay precedes all of the light particle emission. The solid line shows the predicted velocities assuming that the binary decay follows all of the light particle emission (see text).

Fig. 16. Emission velocity distributions for Z = 6 fragments from the 80 MeV/u $^{139}La + ^{12}C$ reaction at angles of 25°, 155°, and 165° in the source frame. The distribution at 165° has been multiplied by a factor of 10.

Fig. 17. Angular distributions ($d\sigma/d\theta$) in the source frame for representative Z-values from the 80 and 100 MeV/u $^{139}La + ^{12}C$ reactions. The Z-value and normalization factor are indicated for each set of points. The solid lines show the fits to the distributions used to extract the absolute cross sections. At emission angles near 90°, the lighter complex fragments are emitted to larger laboratory angles than covered by the detection array, so differential cross sections were not measured.

Fig. 18. The ratio of fragments emitted forward of 90° to those emitted backward of 90° (in the source frame), as a function of Z-value, for the 50, 80, and 100 MeV/u $^{139}La + ^{12}C$ reactions. The solid lines are linear fits to the log of the ratios. The arrows indicate the average Z-values corresponding to symmetric decay as determined by the coincidence data, $\langle Z \rangle = \frac{1}{2}(\overline{Z_1+Z_2})$. The dashed line (= 1) corresponds to forward/backward symmetry.

Fig. 19. Angle-integrated cross sections of products from the 18[25]), 50, 80, and 100 MeV/u $^{139}La + ^{12}C$ reactions. Error bars are shown where the statistical error exceeds the size of the data points. The solid lines through each set of data guide the eye.

Fig. 20. Distributions of Z_{Total} for 2-fold, 3-fold, and 4-fold complex fragment (Z > 2) events from the 80 and 100 MeV/u $^{139}La + ^{12}C$ reactions.

Fig. 21. The average charge loss from coincidence events $[(Z_{Projectile} + Z_{Target}) - \overline{(Z_1 + Z_2)}]$ as a function of the center-of-mass energy in the $^{139}La + ^{12}C$ system. The solid line is a linear fit to the data points.

Fig. 22. The measured average charge loss (solid points) for coincidence events $[(Z_{Projectile} + Z_{Target}) - \overline{(Z_1 + Z_2)}]$, as a function of the Z-value of one of the fragments, from the 50, 80, and 100 MeV/u $^{139}La + ^{12}C$ reactions. The solid line is the prediction from a statistical decay code (GEMINI[22]) incorporating both complex fragment emission and light particle evaporation (see text). The dashed line is the prediction from the statistical evaporation code PACE[46]), assuming that the binary decay occurs prior to the light particle evaporation.

Fig. 23. Experimental complex fragment cross sections compared to predictions from the compound-nuclear statistical-decay model GEMINI[22]) (see text) for the 50, 80, and 100 MeV/u $^{139}La + ^{12}C$ reactions. The total measured cross sections are shown for those Z-values near symmetry (solid points). For fragments from more asymmetric decays, in which non-equilibrium processes are expected to contribute to the measured cross sections, only the 90^{o} symmetric portion of the cross section is plotted (open circles). The statistical model predictions are shown as the histograms. The statistical uncertainties in the experimental data are smaller than the data points. The statistical uncertainties associated with the Monte Carlo nature of the calculations are approximately 5%.

Fig. 24. Experimental $d\sigma/d\theta$ angular distributions (points) in the source frame compared to predictions from the compound statistical decay model GEMINI[22]) (histograms) for several Z-values from the 80 and 100 MeV/u $^{139}La + ^{12}C$ reactions. The Z-value is indicated for each set of data. Normalization factors are indicated for those data sets that have been scaled. The statistical uncertainties in the experimental data are smaller than the data points. The statistical uncertainties associated with the Monte Carlo nature of the calculations are approximately 10%.

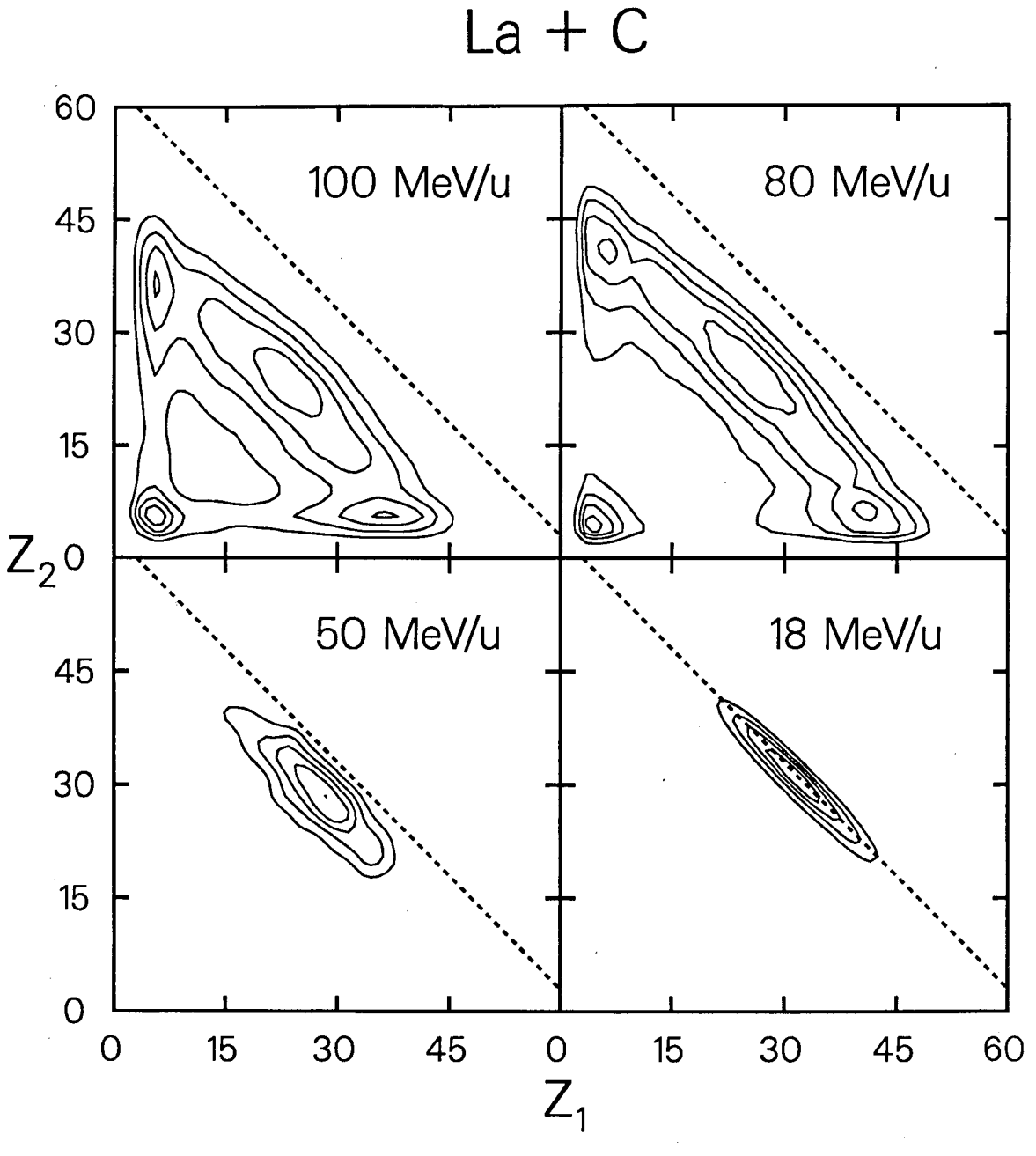
La + C
100 MeV/u
80 MeV/u
50 MeV/u
18 MeV/u
Z_2
Z_1
0
15
30
45
60
XBL 896-2514

Figure 1

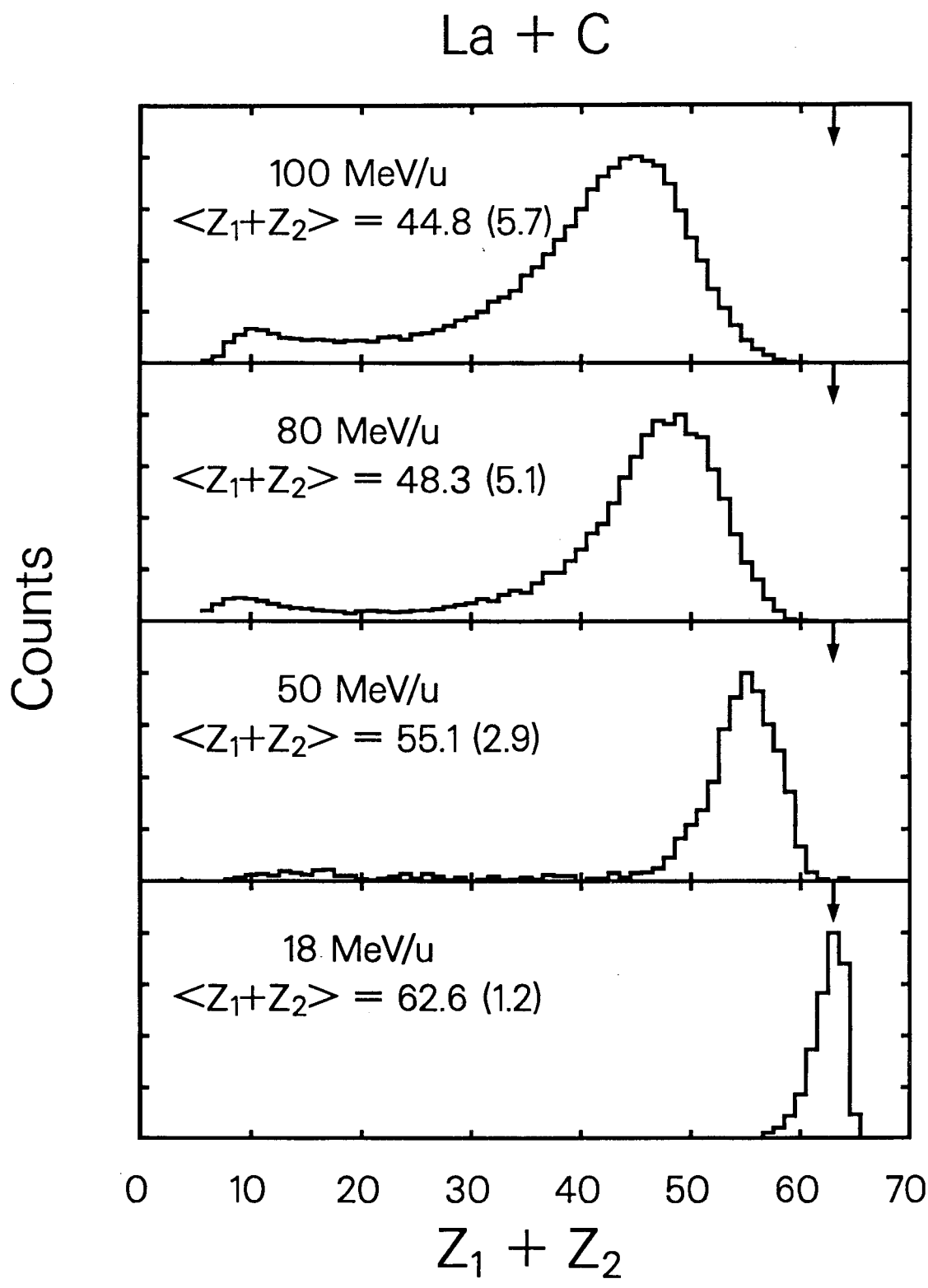
La + C
100 MeV/u
<Z1+Z2> = 44.8 (5.7)
80 MeV/u
<Z1+Z2> = 48.3 (5.1)
50 MeV/u
<Z1+Z2> = 55.1 (2.9)
18 MeV/u
<Z1+Z2> = 62.6 (1.2)
Counts
0
10
20
30
40
50
60
70
Z1 + Z2
XBL 896-2513

Figure 2

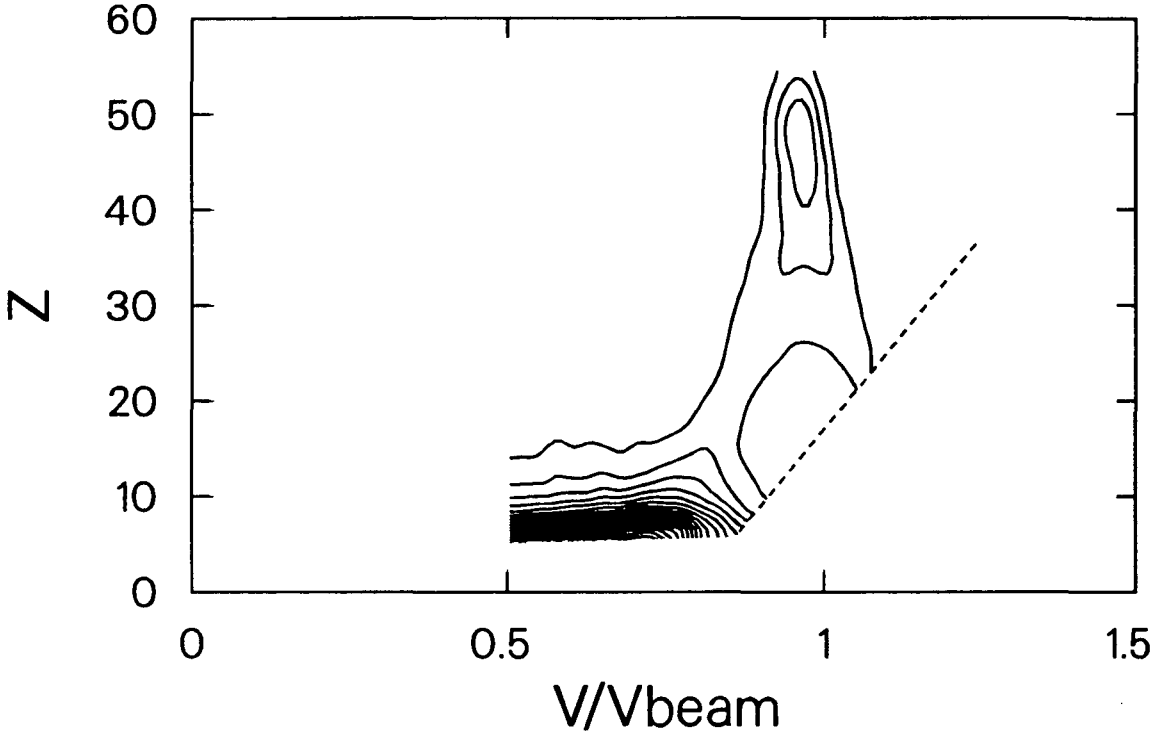

XBL 8611-4289 A

Figure 3

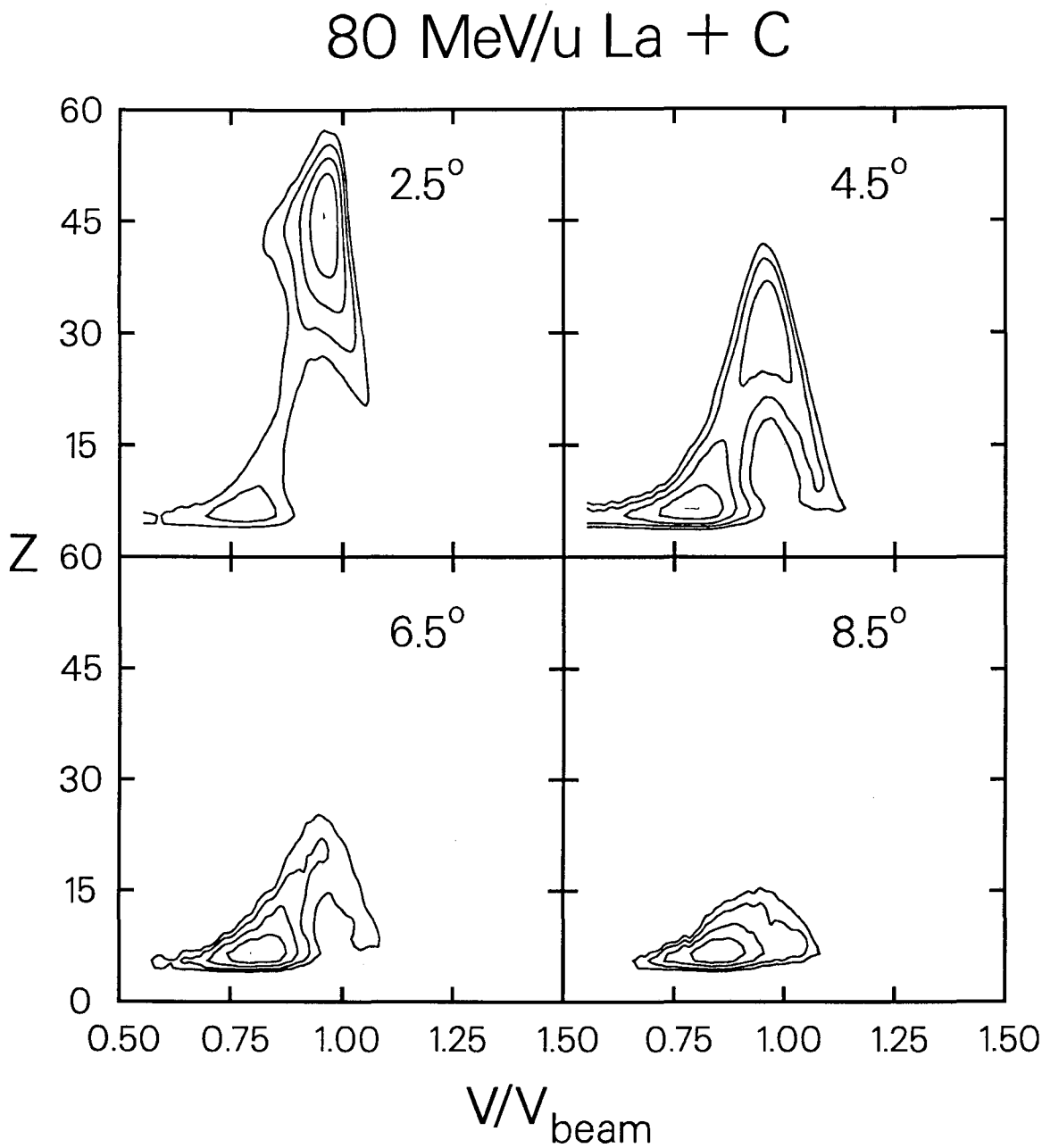

XBL 896-2511

Figure 4

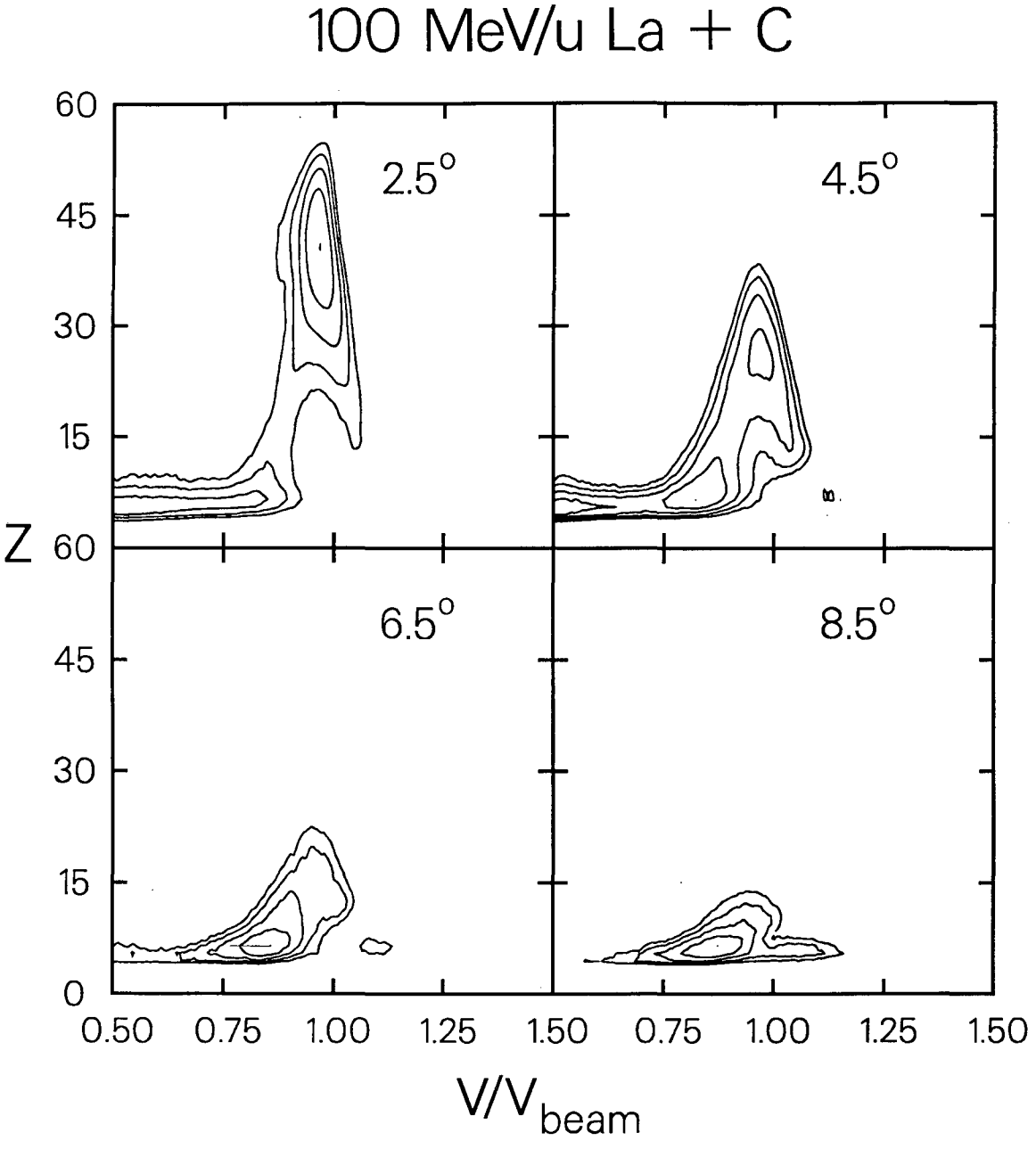

XBL 896-2512

Figure 5

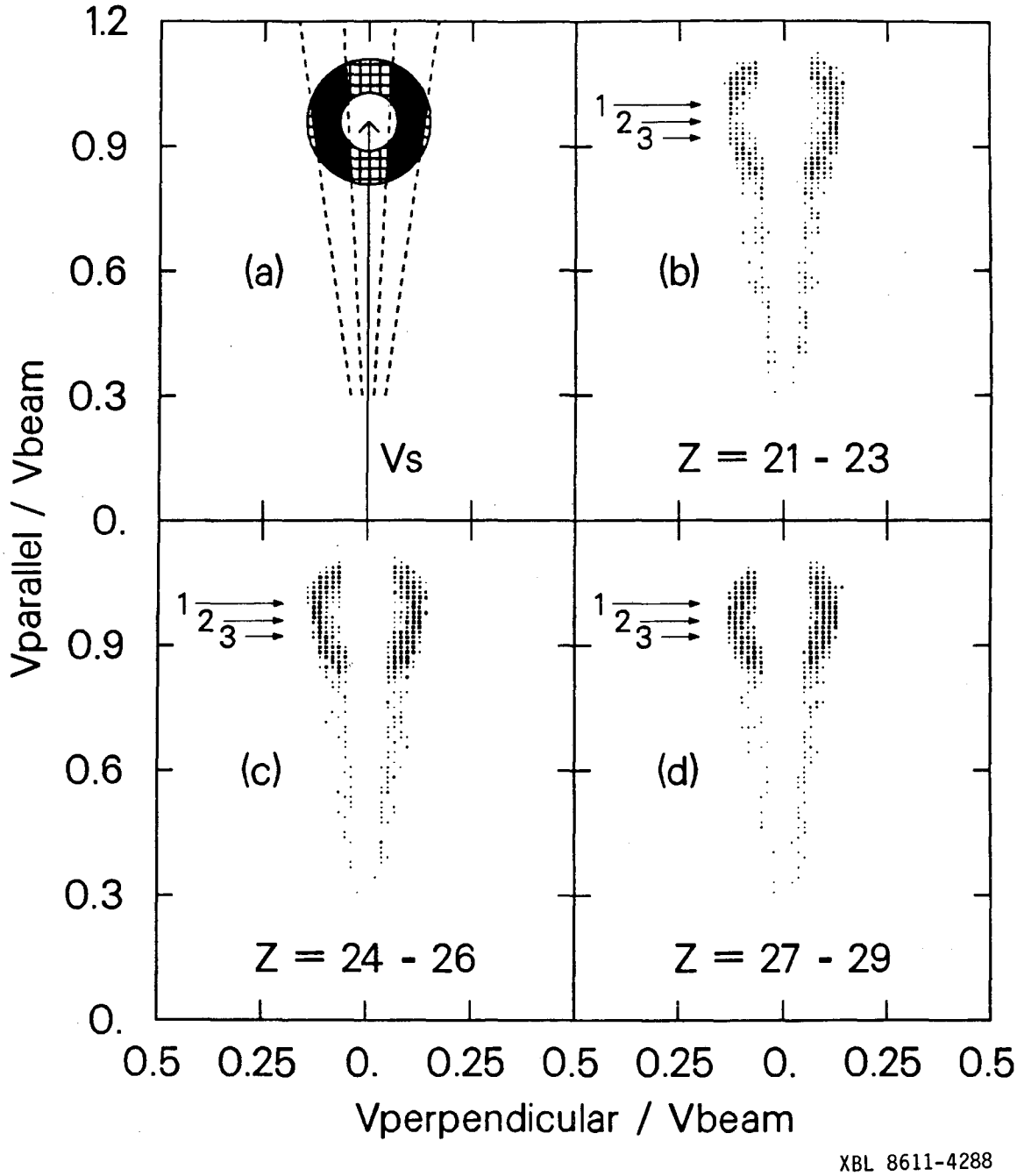
1.2
0.9
0.6
0.3
0.
(a)
Vs
(b)
Z = 21 - 23
1
2
3
(c)
Z = 24 - 26
(d)
Z = 27 - 29
0.5 0.25 0. 0.25 0.5 0.25 0. 0.25 0.5
Vparallel / Vbeam
Vperpendicular / Vbeam
XBL 8611-4288

Figure 6

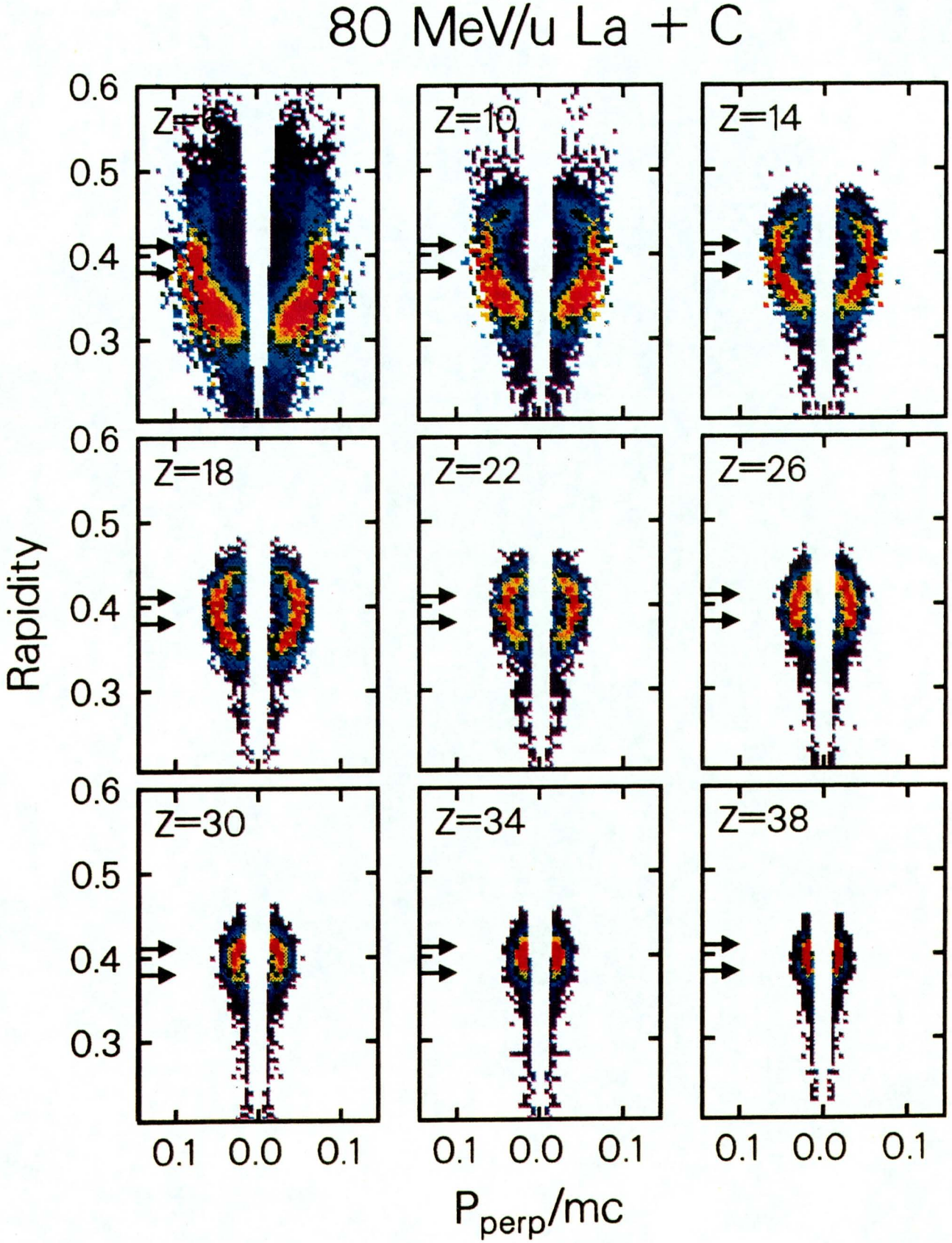
80 MeV/u La + C
Z=6
Z=10
Z=14
Z=18
Z=22
Z=26
Z=30
Z=34
Z=38
Rapidity
0.6
0.5
0.4
0.3
0.1
0.0
0.1
P perp/mc

Figure 7

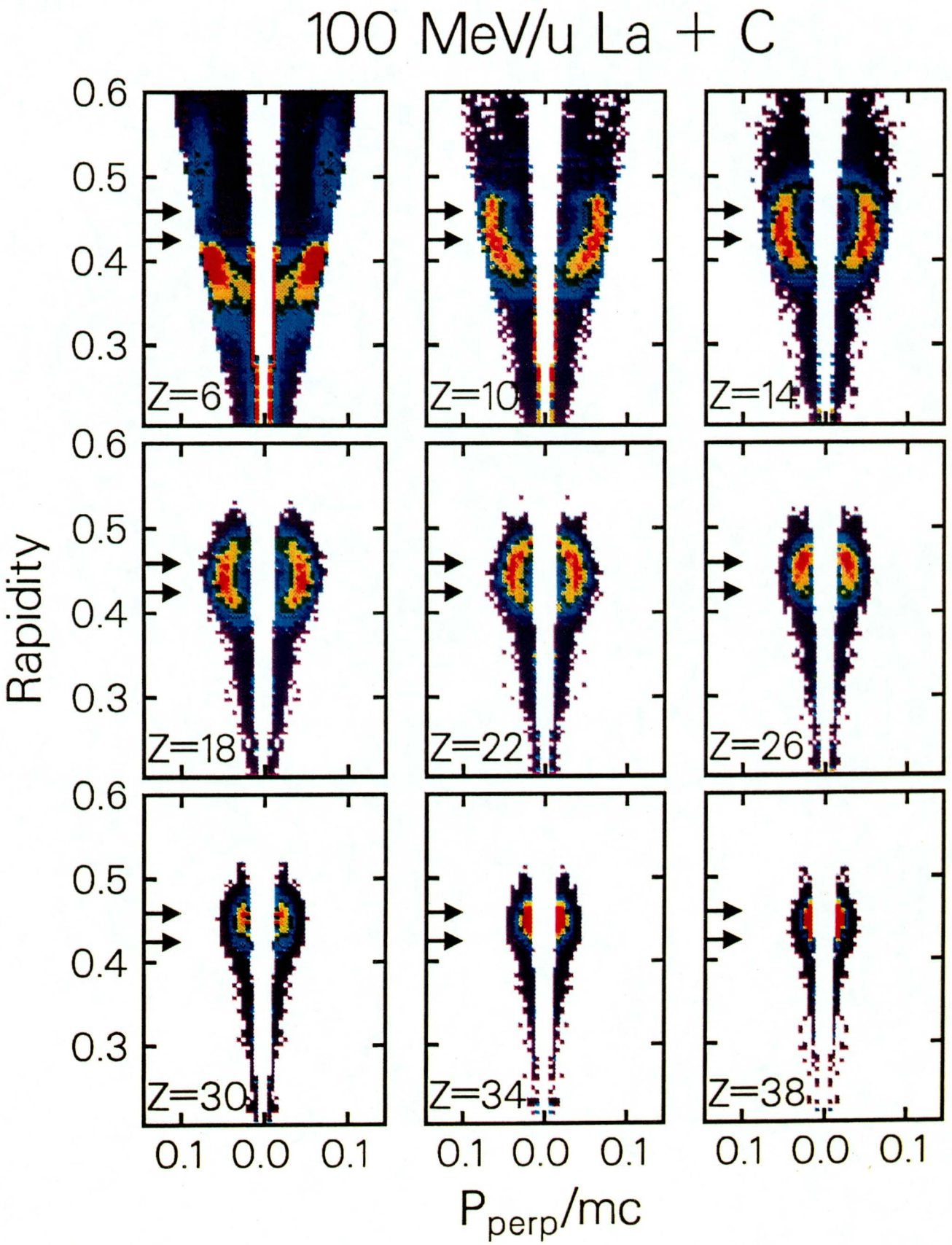
100 MeV/u La + C
Rapidity
0.6
0.5
0.4
0.3
Z=6
Z=10
Z=14
Z=18
Z=22
Z=26
Z=30
Z=34
Z=38
0.1 0.0 0.1
P perp/mc

Figure 8

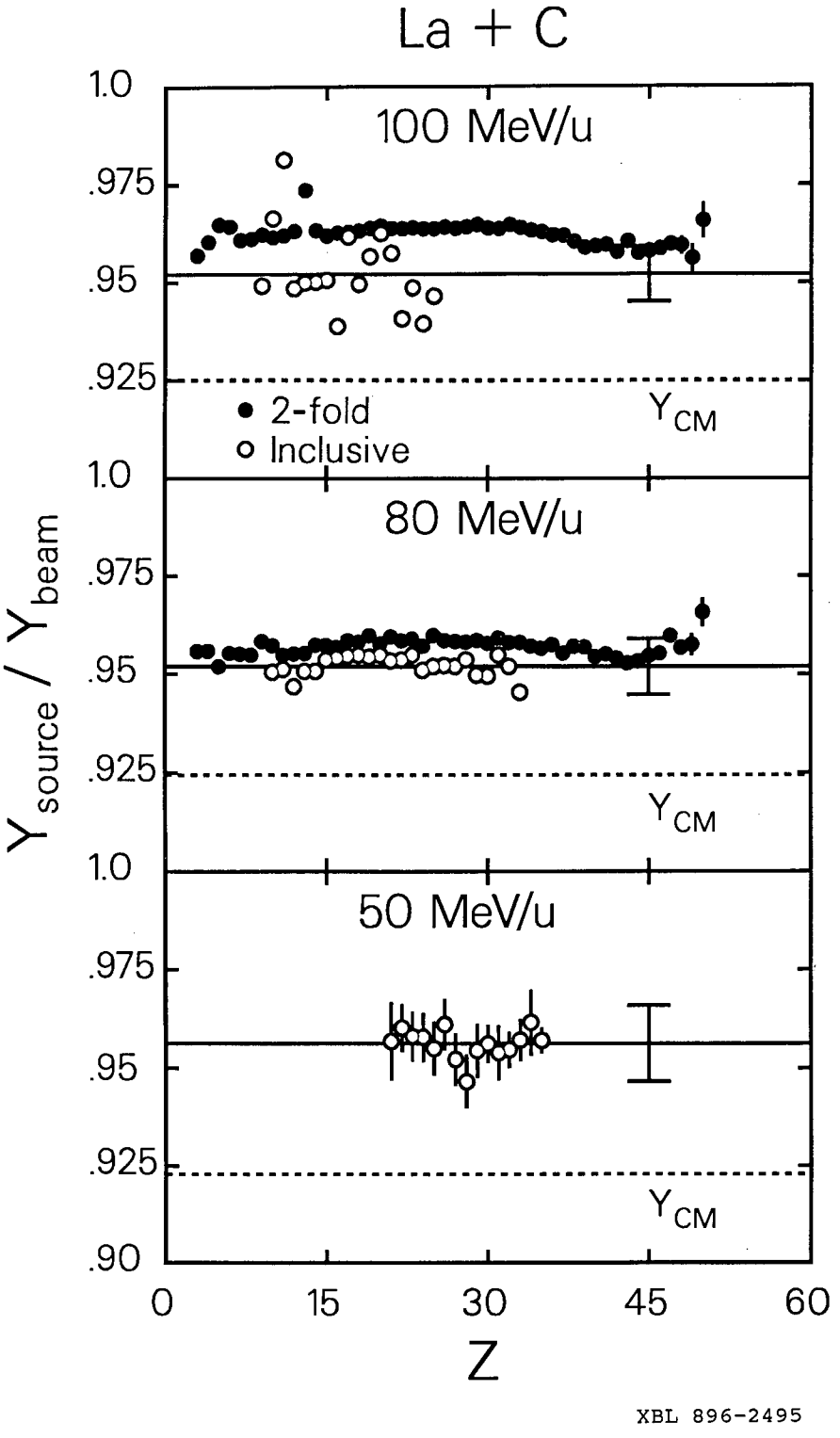
La + C
100 MeV/u
80 MeV/u
50 MeV/u
2-fold
Inclusive
Y_{CM}
Y_{source} / Y_{beam}
Z
1.0
.975
.95
.925
.90
0
15
30
45
60
XBL 896-2495

Figure 9

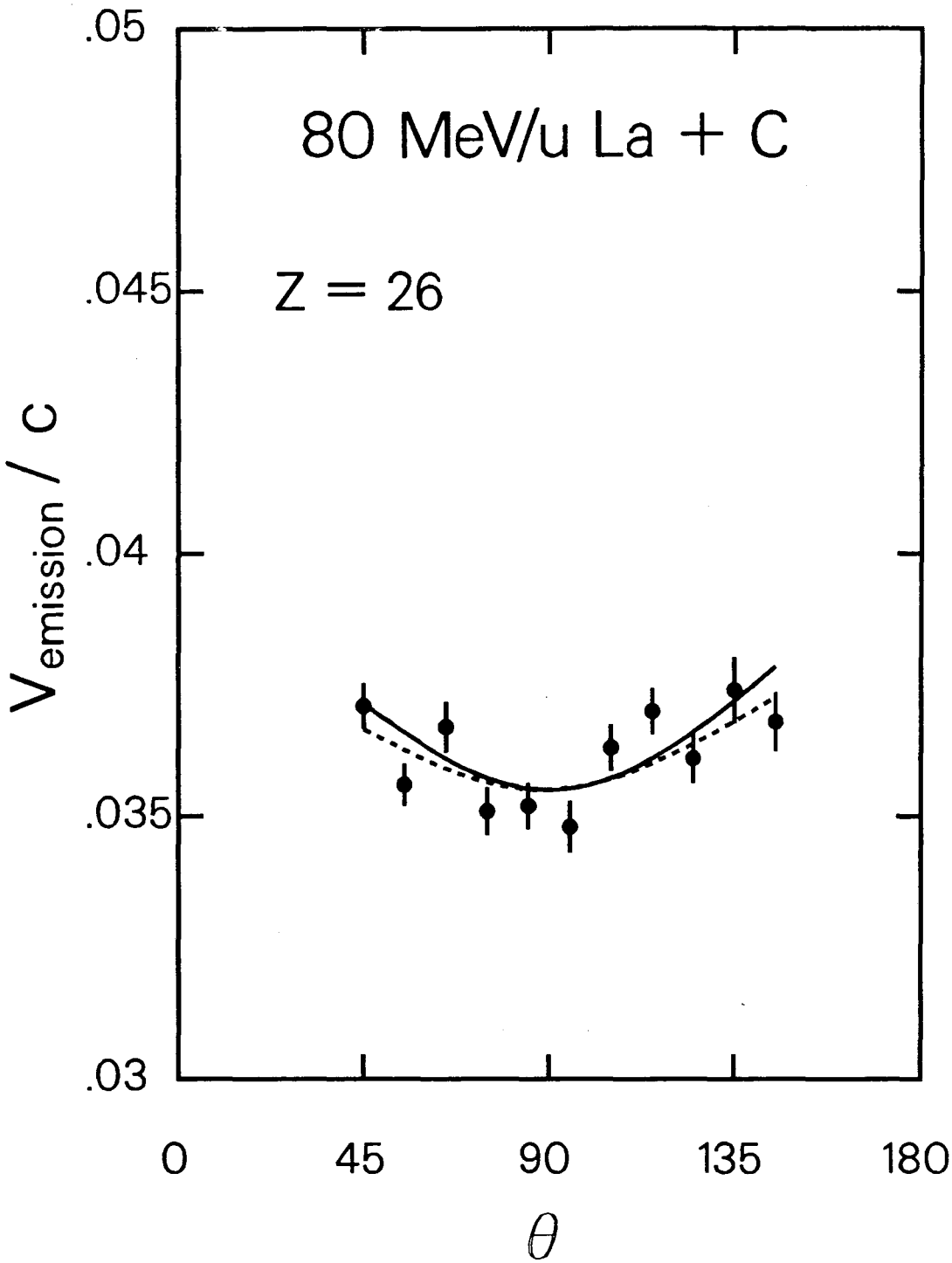

XBL 896-2497

Figure 10

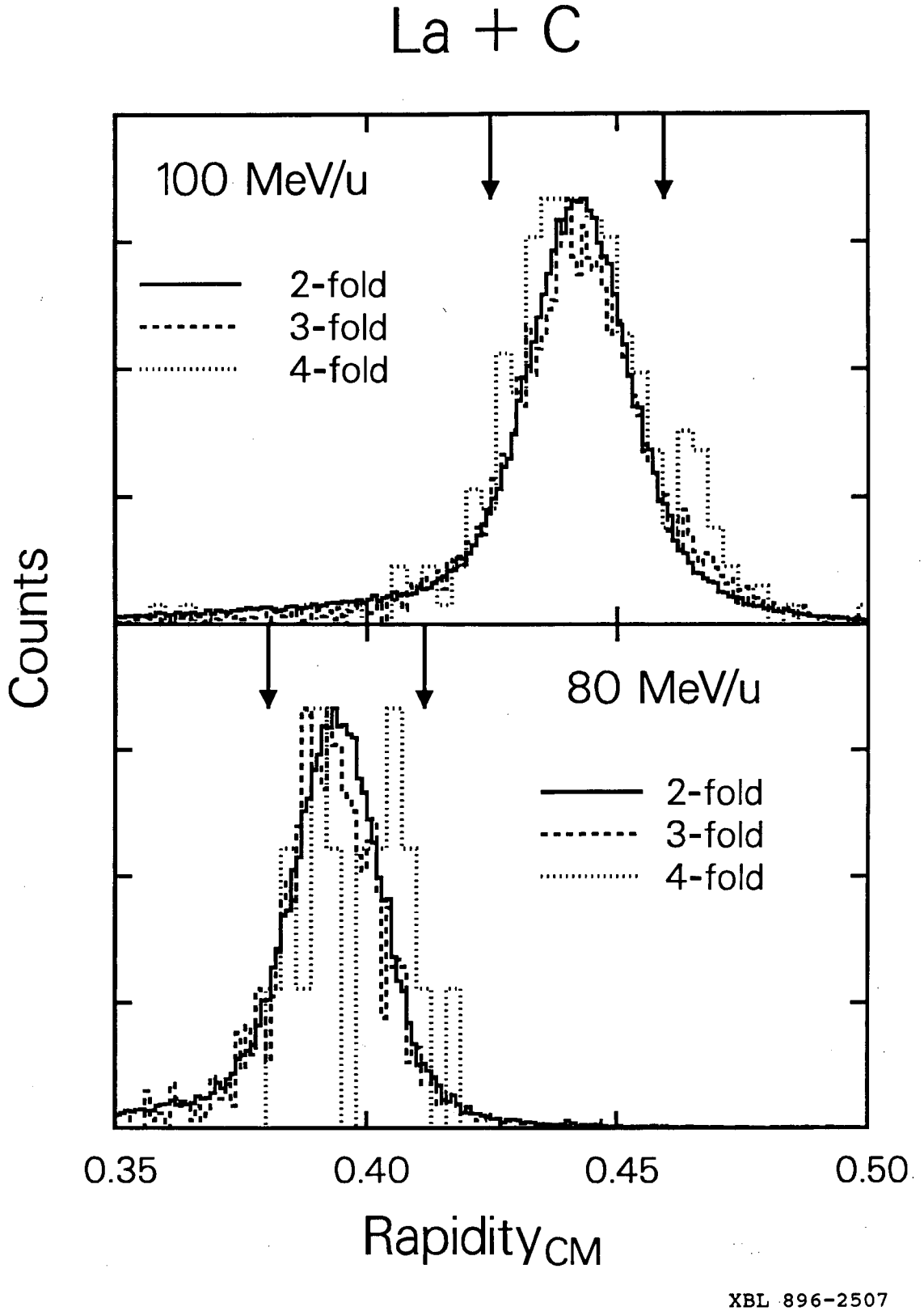
La + C
100 MeV/u
2-fold
3-fold
4-fold
80 MeV/u
2-fold
3-fold
4-fold
Counts
0.35
0.40
0.45
0.50
Rapidity$_{CM}$
XBL 896-2507

Figure 11

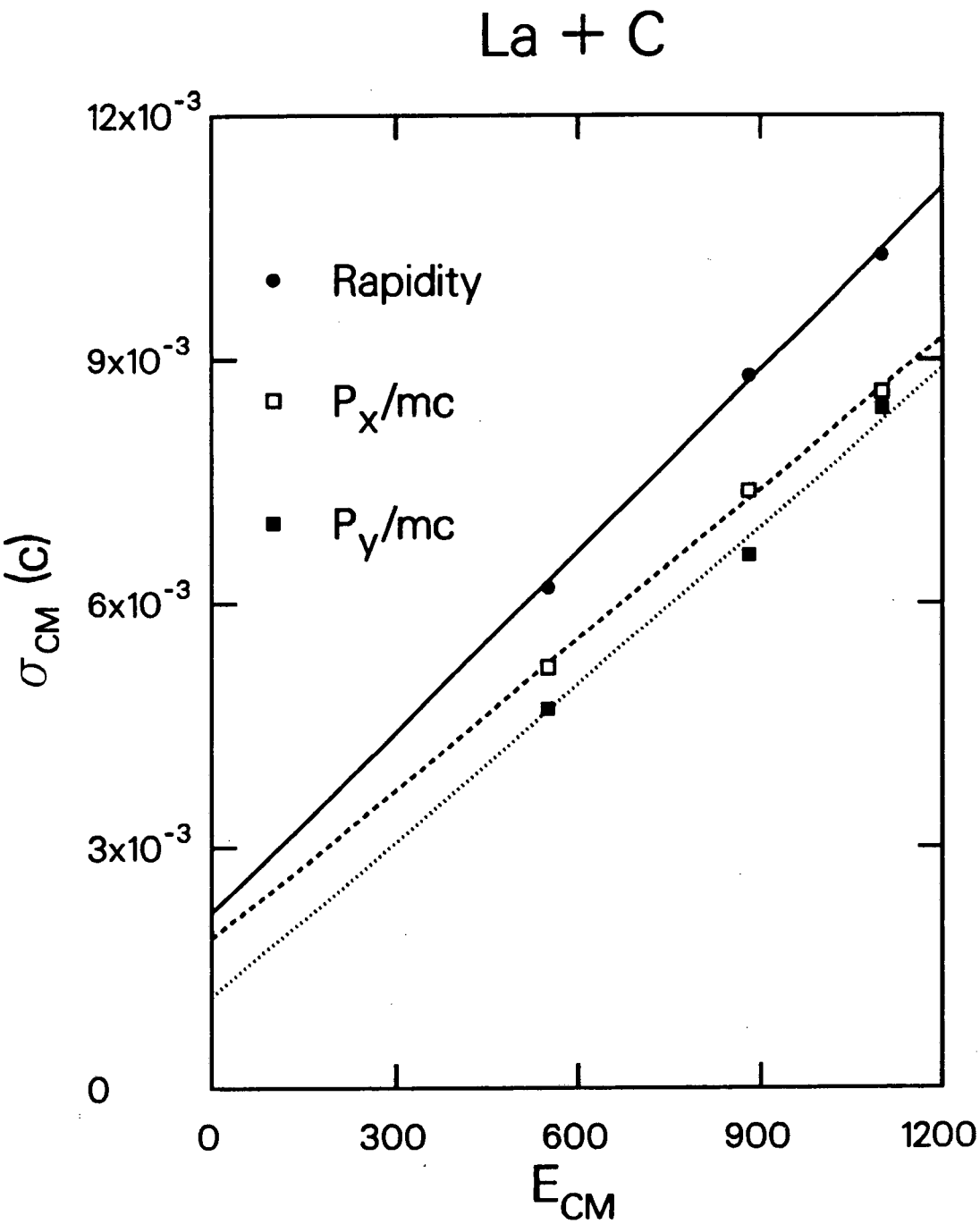

XBL 905-1600

Figure 12

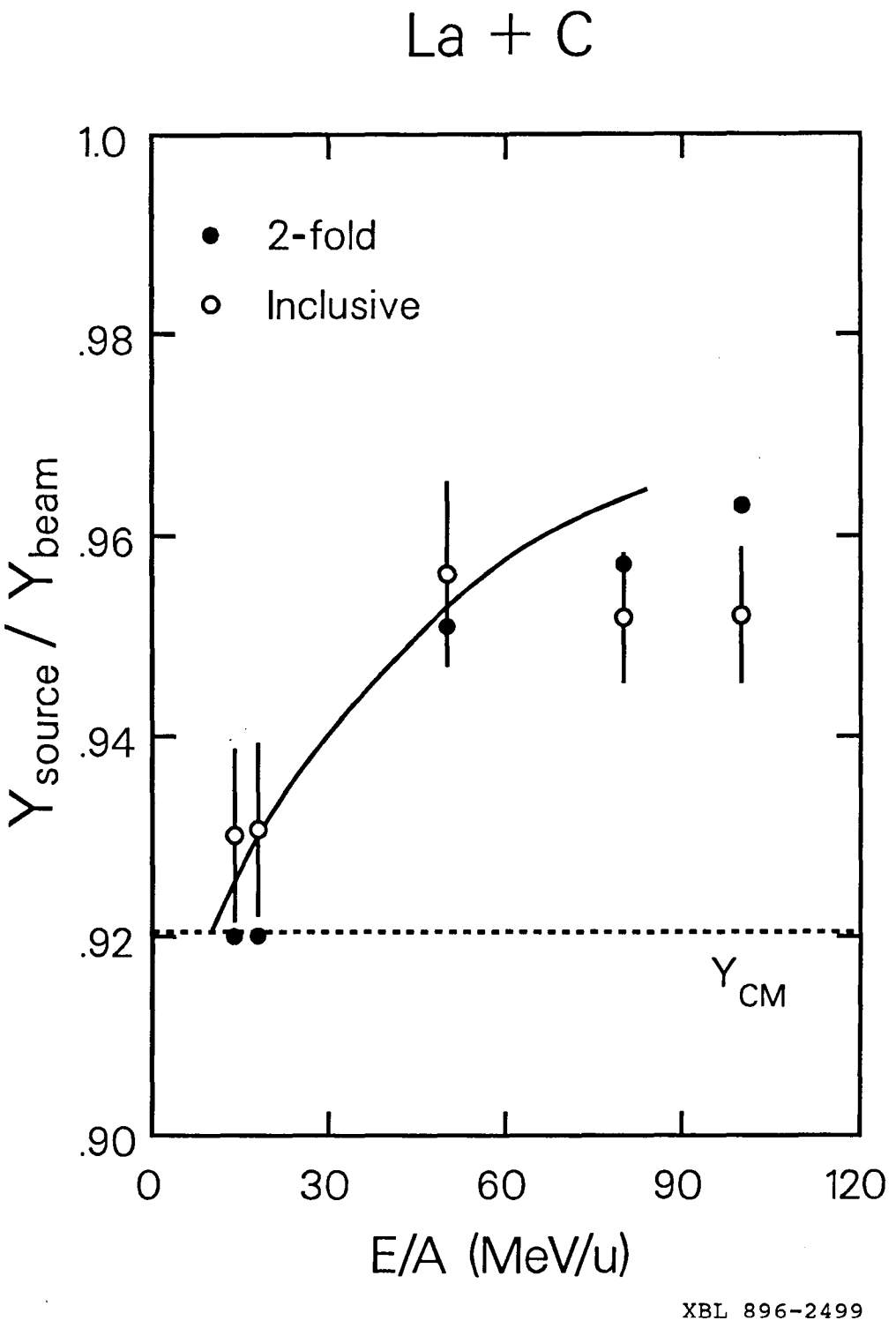
La + C
1.0
.98
.96
.94
.92
.90
2-fold
Inclusive
Y_{source} / Y_{beam}
Y_{CM}
0
30
60
90
120
E/A (MeV/u)
XBL 896-2499

Figure 13

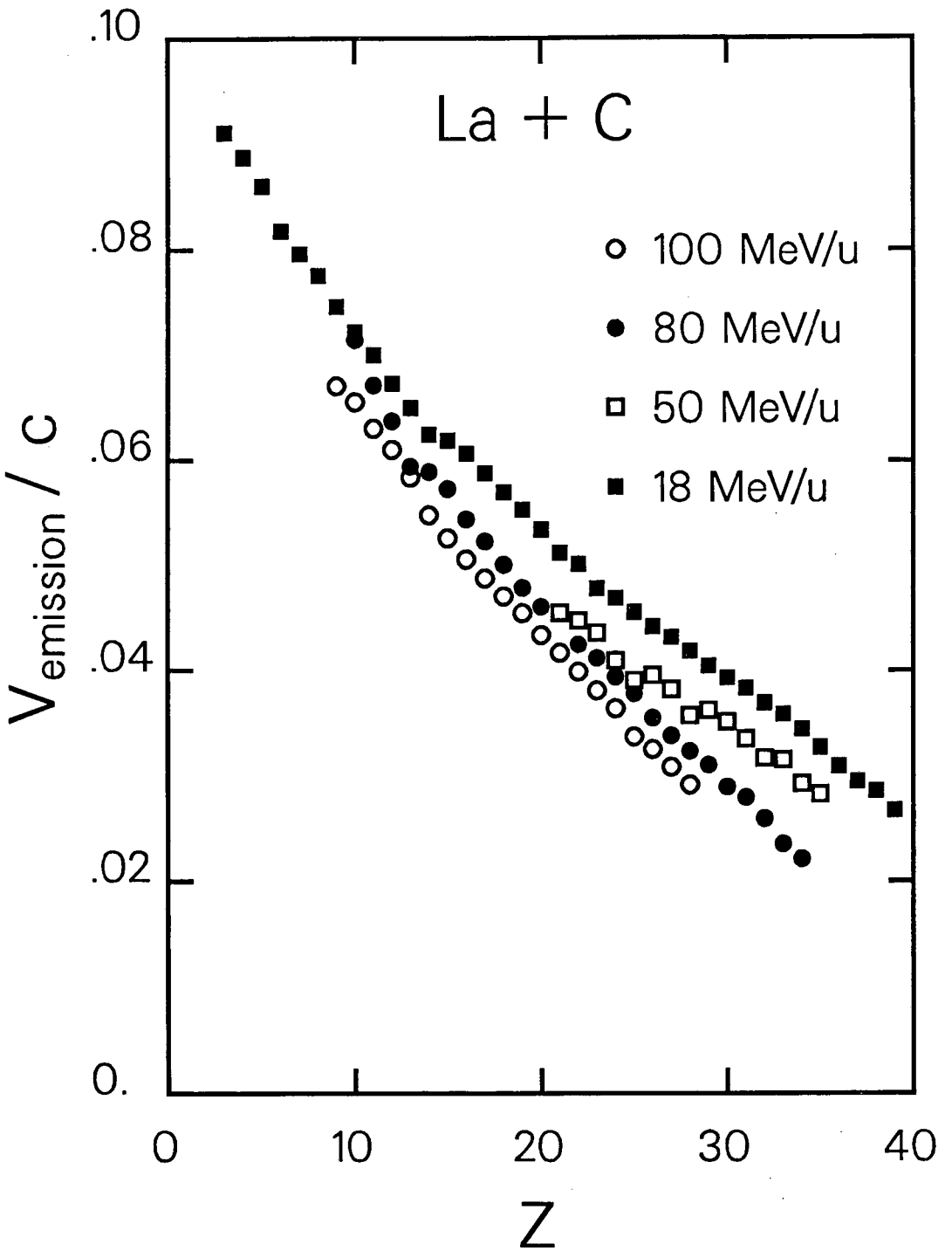
La + C
100 MeV/u
80 MeV/u
50 MeV/u
18 MeV/u
$V_{emission}$ / c
.10
.08
.06
.04
.02
0.
0
10
20
30
40
Z
XBL 896-2500

Figure 14

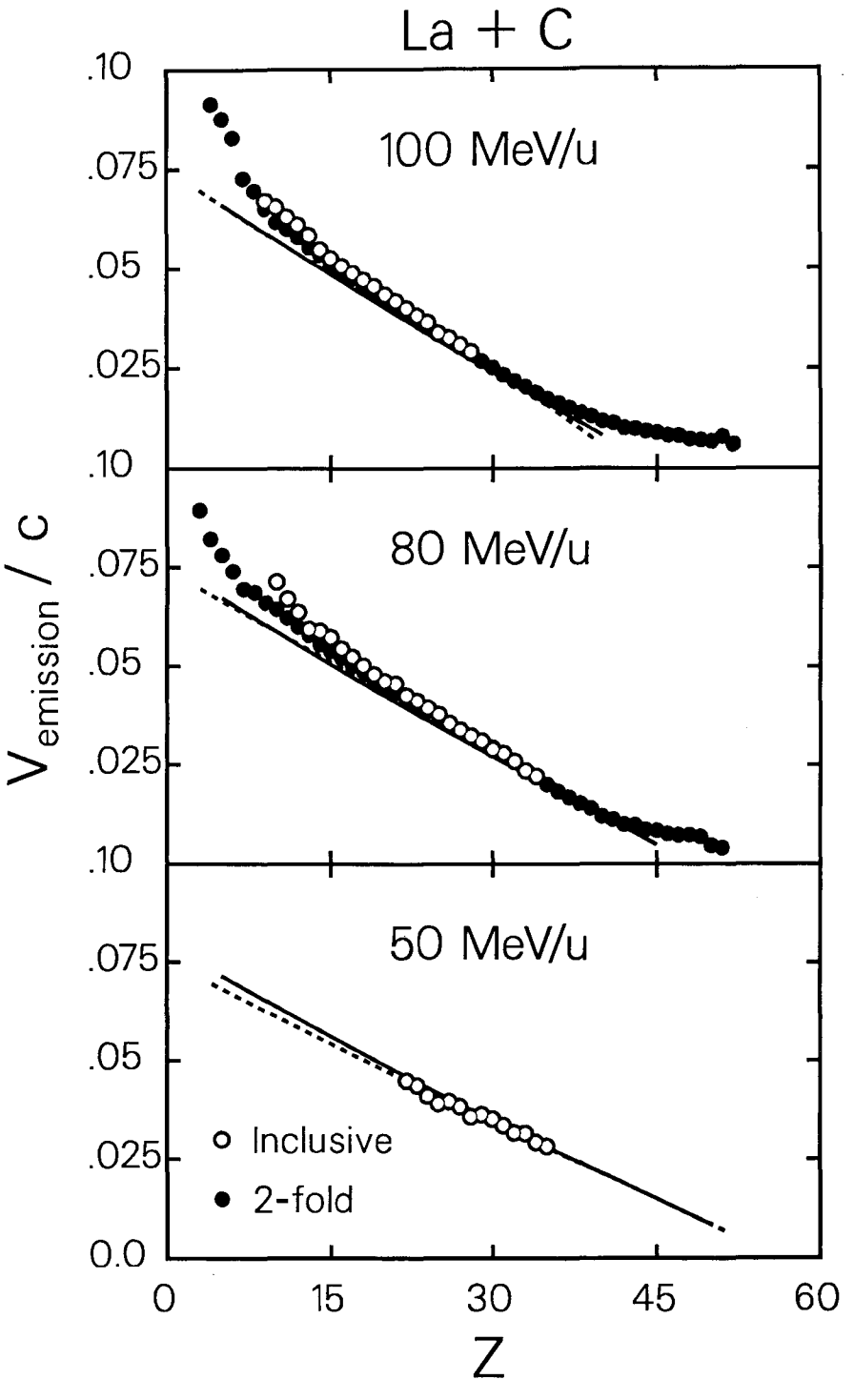
La + C
100 MeV/u
80 MeV/u
50 MeV/u
Inclusive
2-fold
$V_{emission}$ / c
Z
.10
.075
.05
.025
0.0
0
15
30
45
60
XBL 896-2501

Figure 15

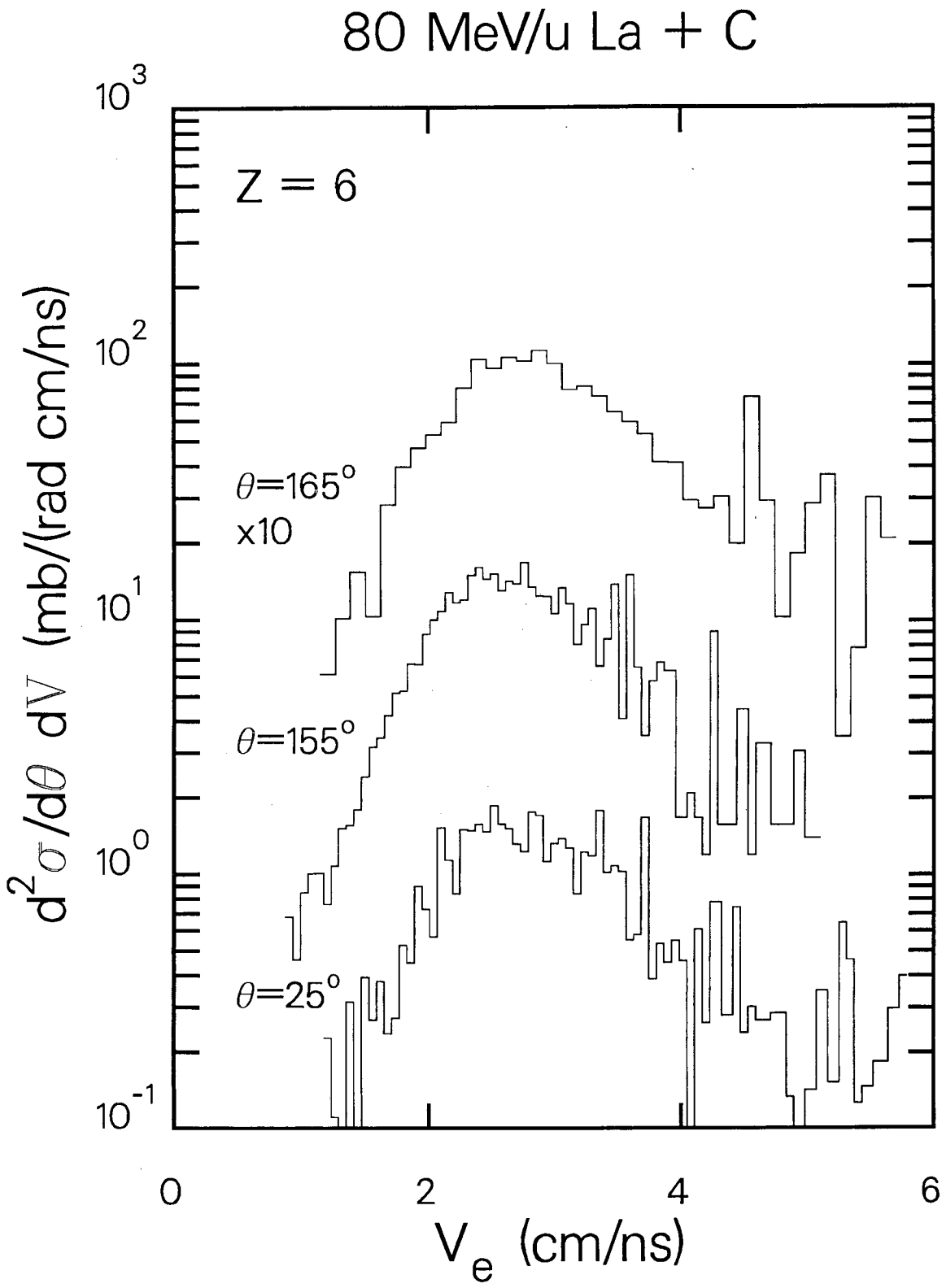

XBL 896-2502

Figure 16

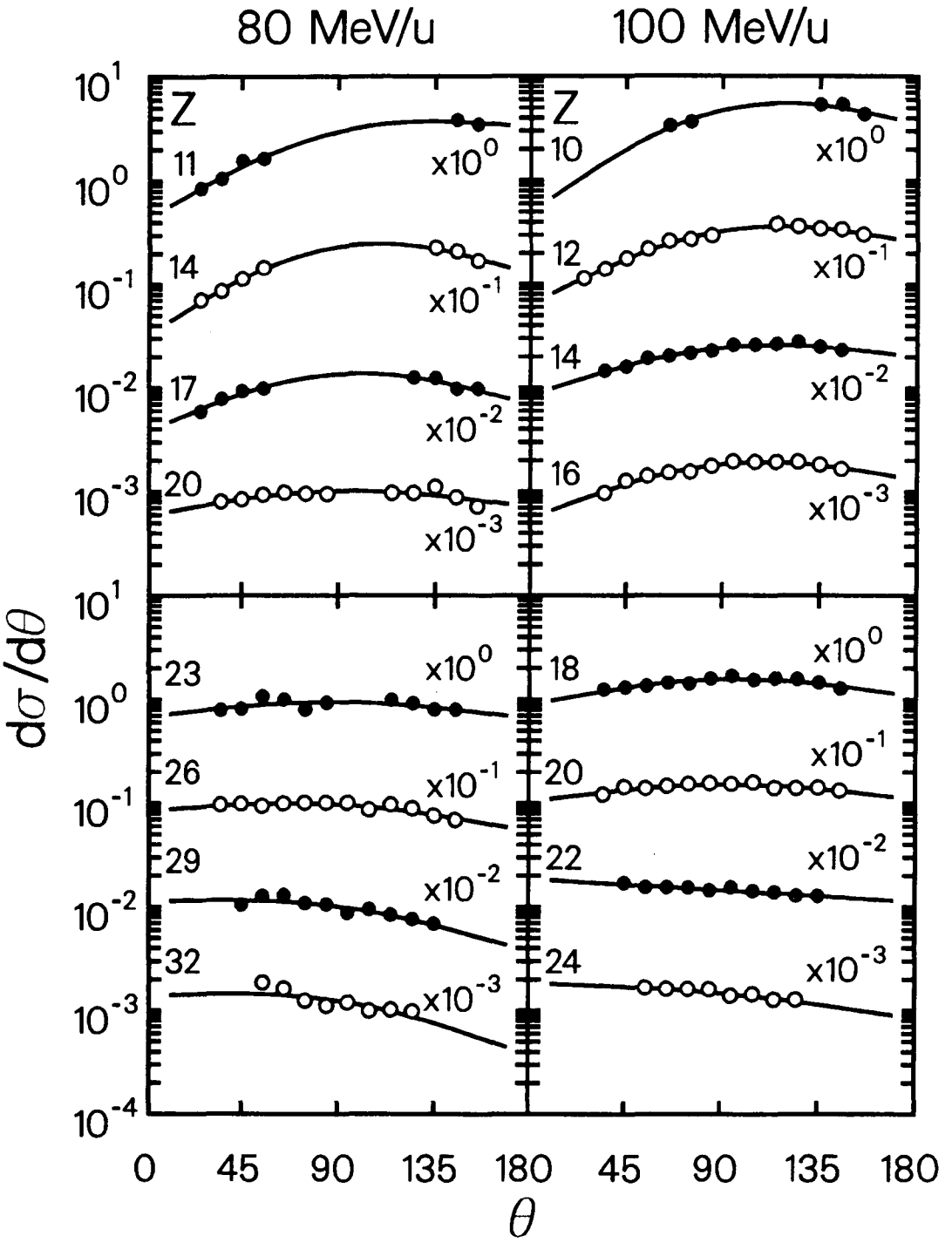
80 MeV/u
100 MeV/u
Z
11
x10^0
14
x10^-1
17
x10^-2
20
x10^-3
Z
10
x10^0
12
x10^-1
14
x10^-2
16
x10^-3
23
x10^0
26
x10^-1
29
x10^-2
32
x10^-3
18
x10^0
20
x10^-1
22
x10^-2
24
x10^-3
dσ/dθ
θ
0
45
90
135
180
45
90
135
180
XBL 901-292

Figure 17

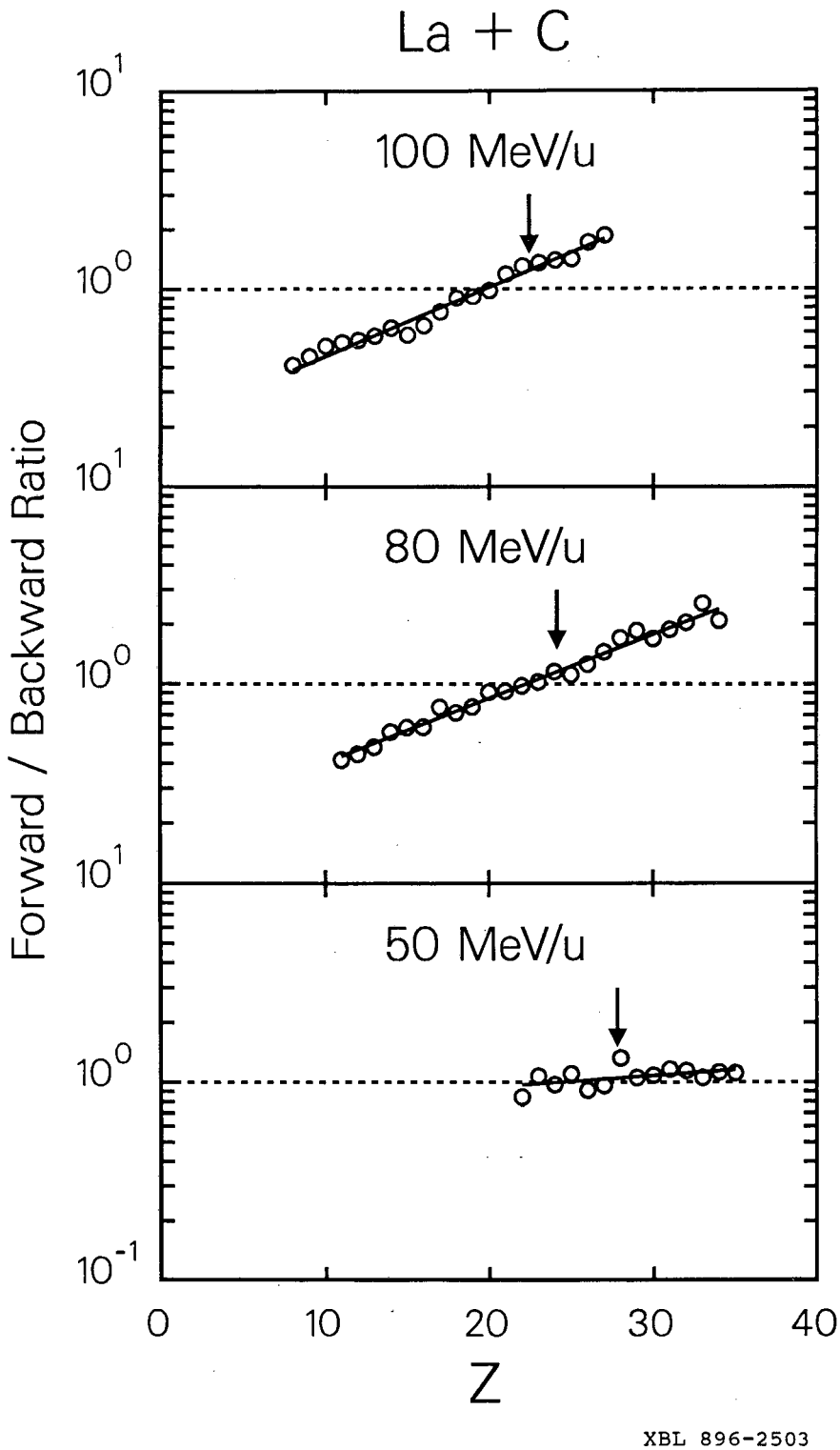
La + C
100 MeV/u
80 MeV/u
50 MeV/u
Forward / Backward Ratio
10^1
10^0
10^1
10^0
10^1
10^0
10^{-1}
0
10
20
30
40
Z
XBL 896-2503

Figure 18

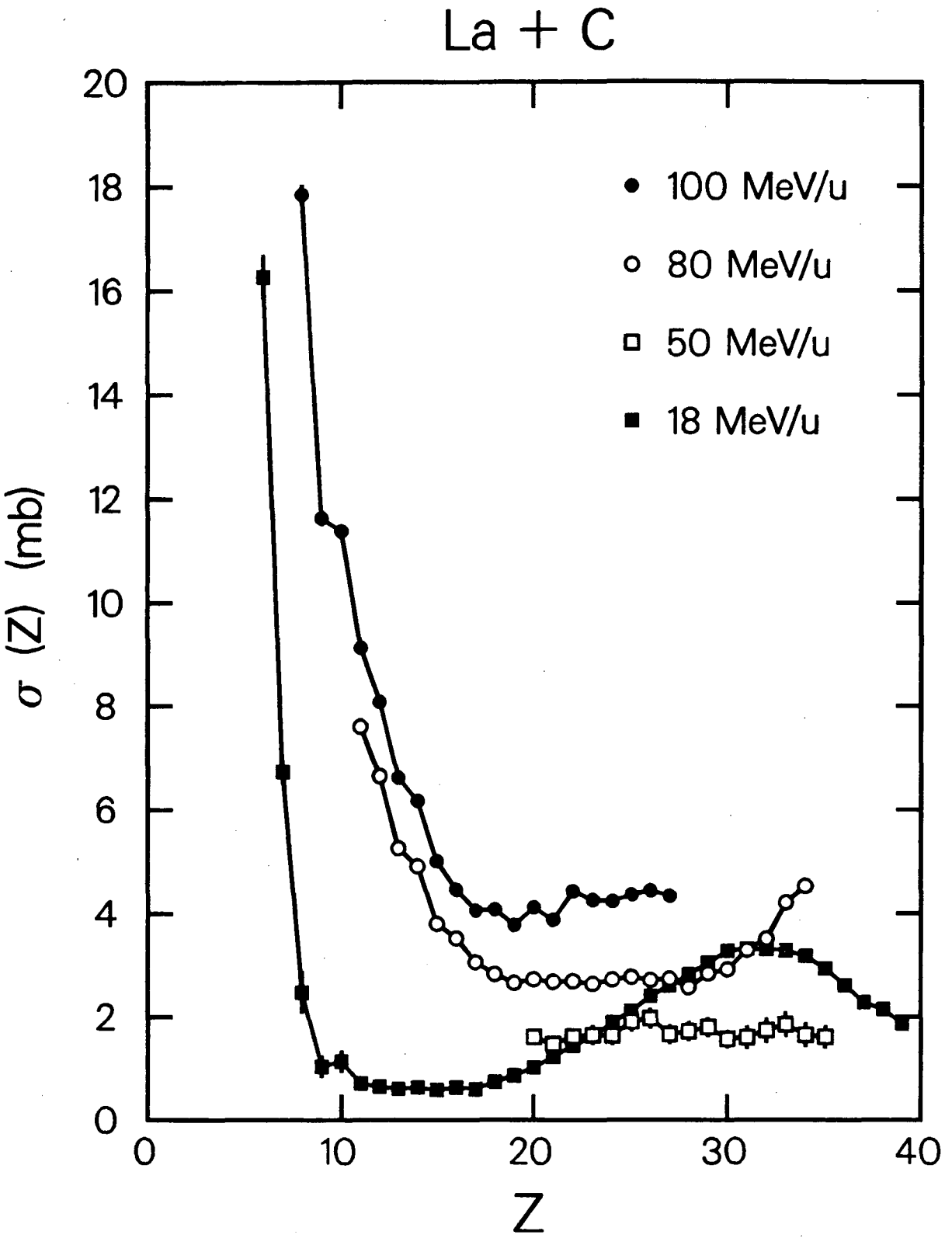

XBL 896-2505 A

Figure 19

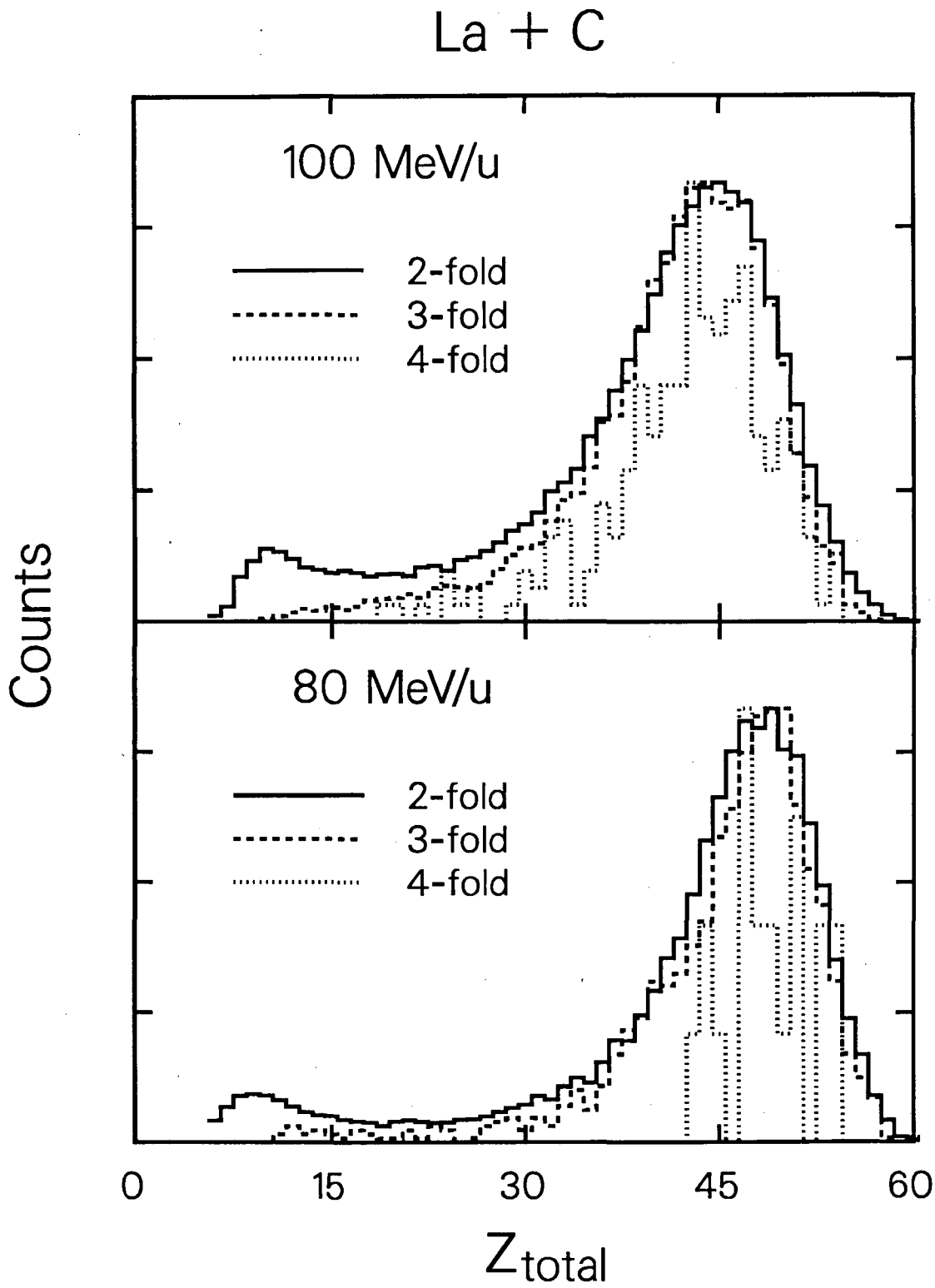
La + C
100 MeV/u
2-fold
3-fold
4-fold
80 MeV/u
2-fold
3-fold
4-fold
Counts
0
15
30
45
60
Ztotal
XBL 896-2506

Figure 20

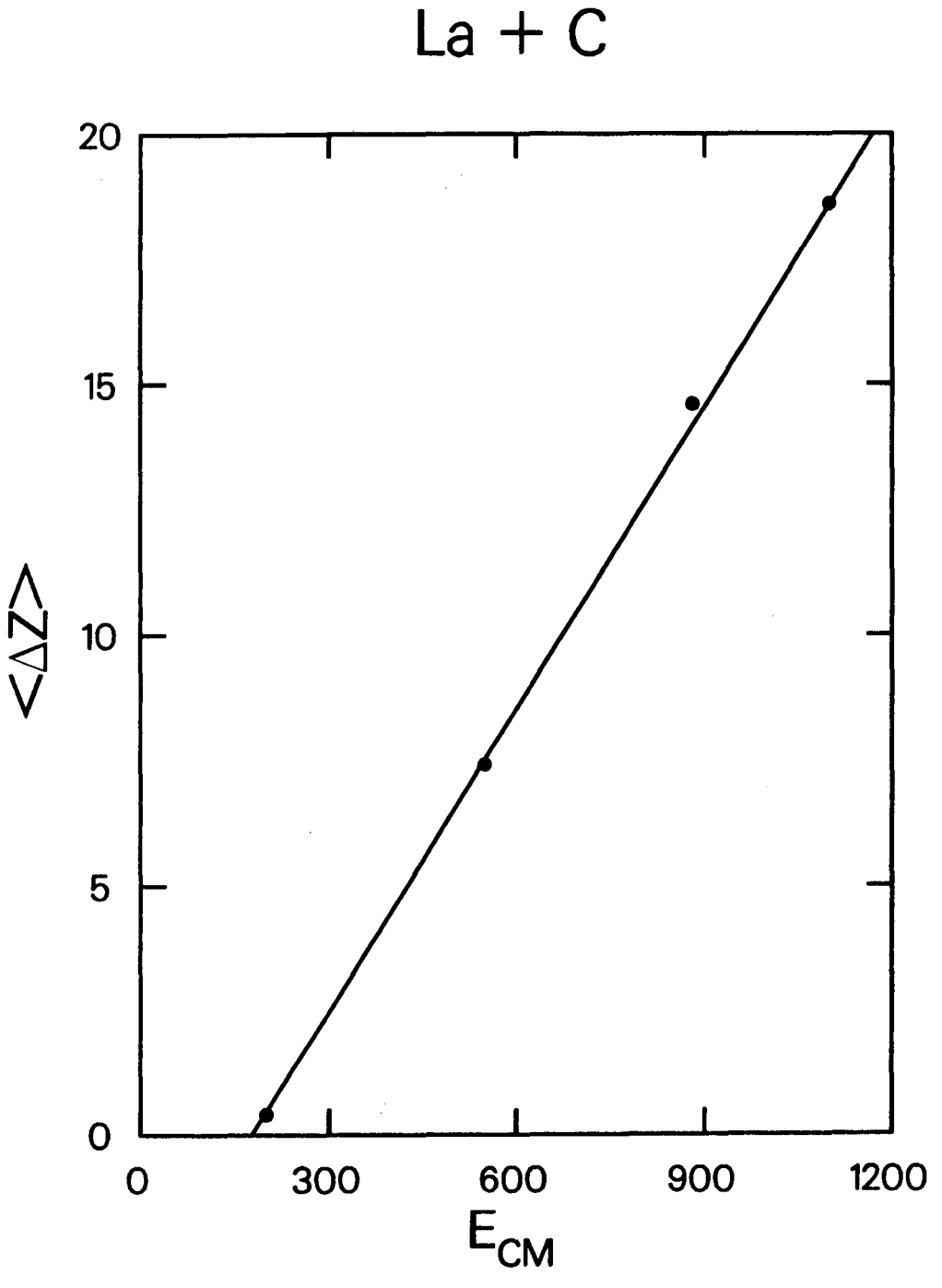

XBL 905-1599

Figure 21

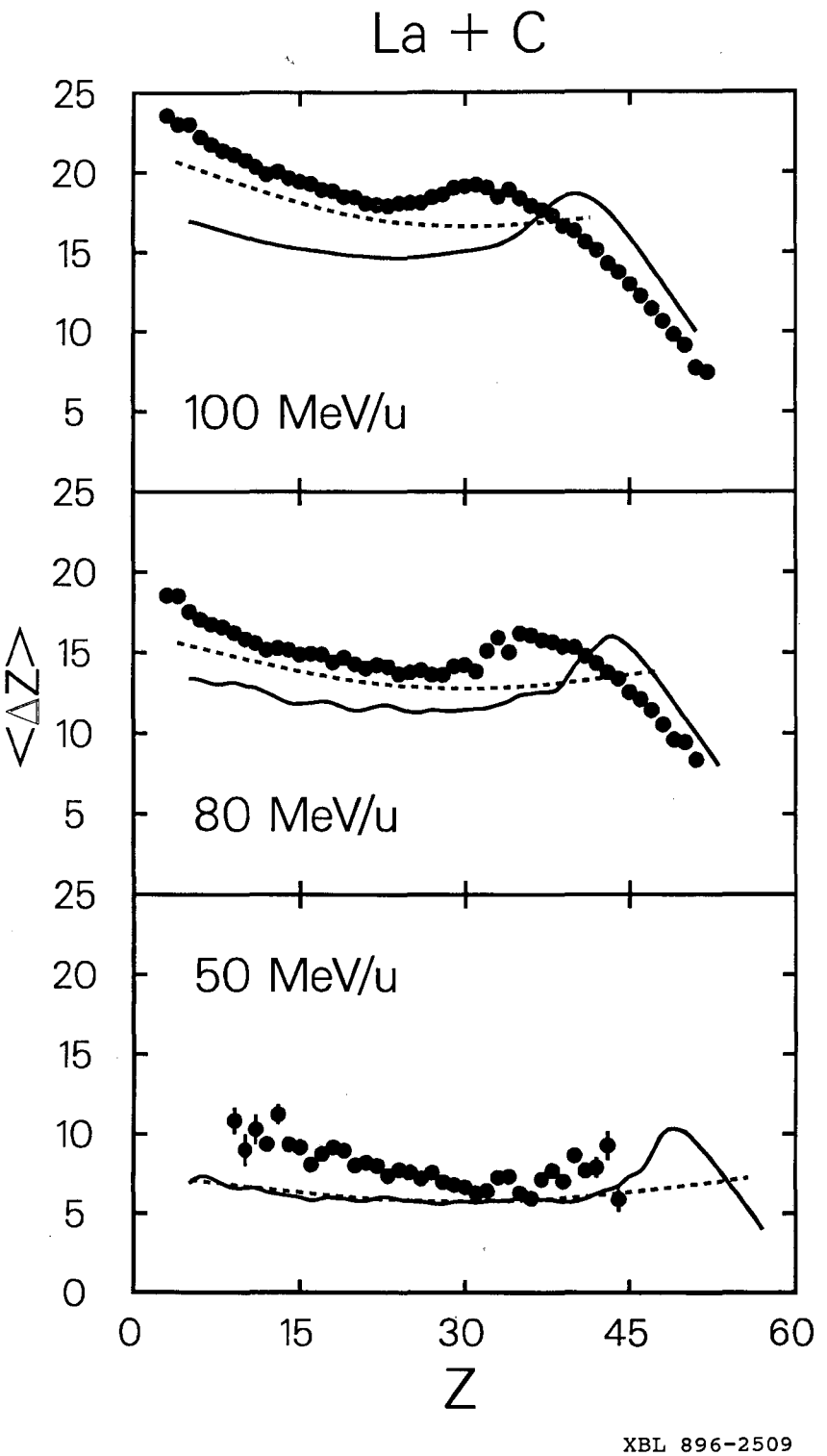
La + C
100 MeV/u
80 MeV/u
50 MeV/u
<ΔZ>
Z
0
15
30
45
60
0
5
10
15
20
25
XBL 896-2509

Figure 22

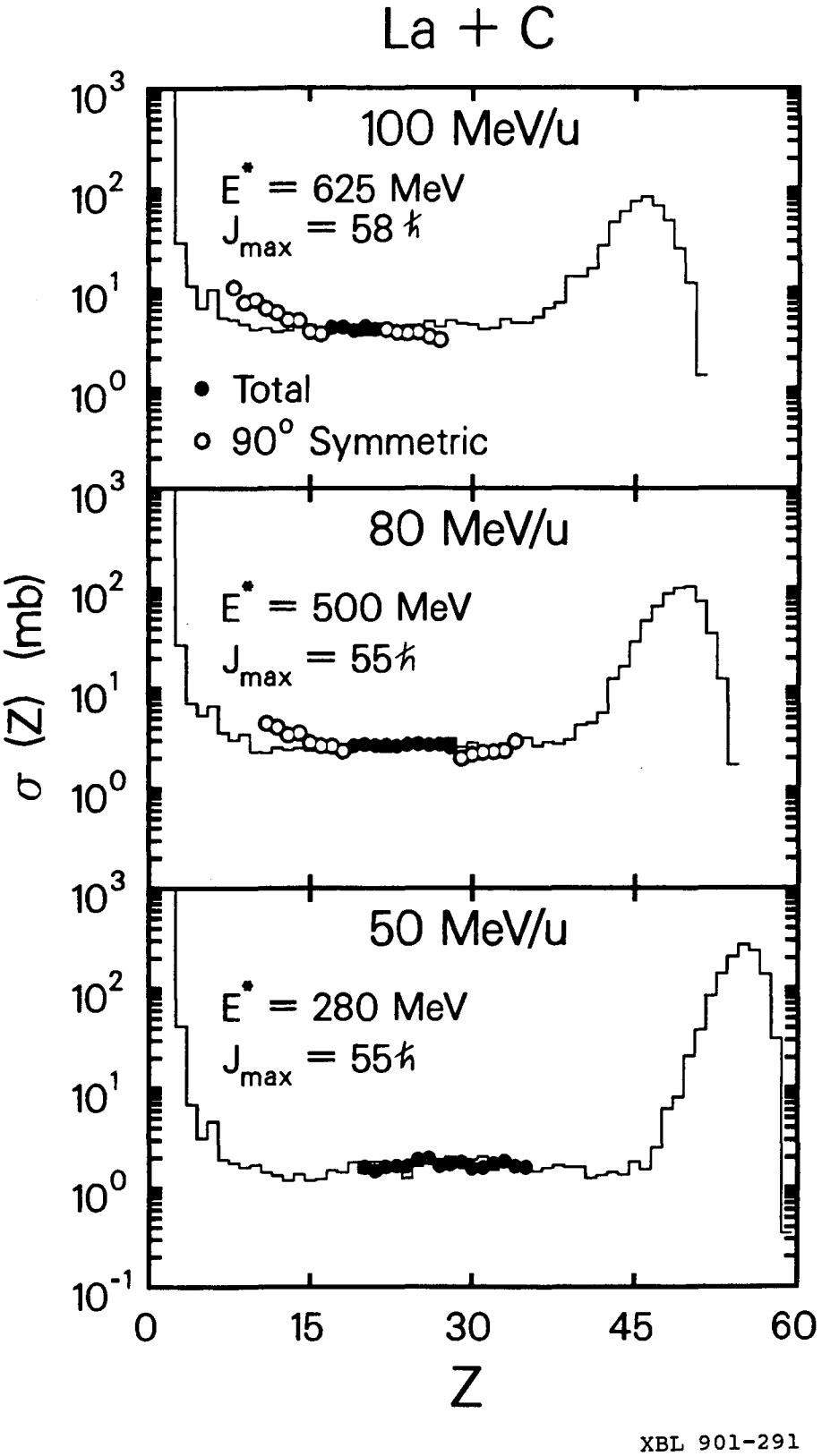
La + C
100 MeV/u
E* = 625 MeV
Jmax = 58 ħ
Total
90° Symmetric
80 MeV/u
E* = 500 MeV
Jmax = 55ħ
50 MeV/u
E* = 280 MeV
Jmax = 55ħ
σ (Z) (mb)
Z
XBL 901-291

Figure 23

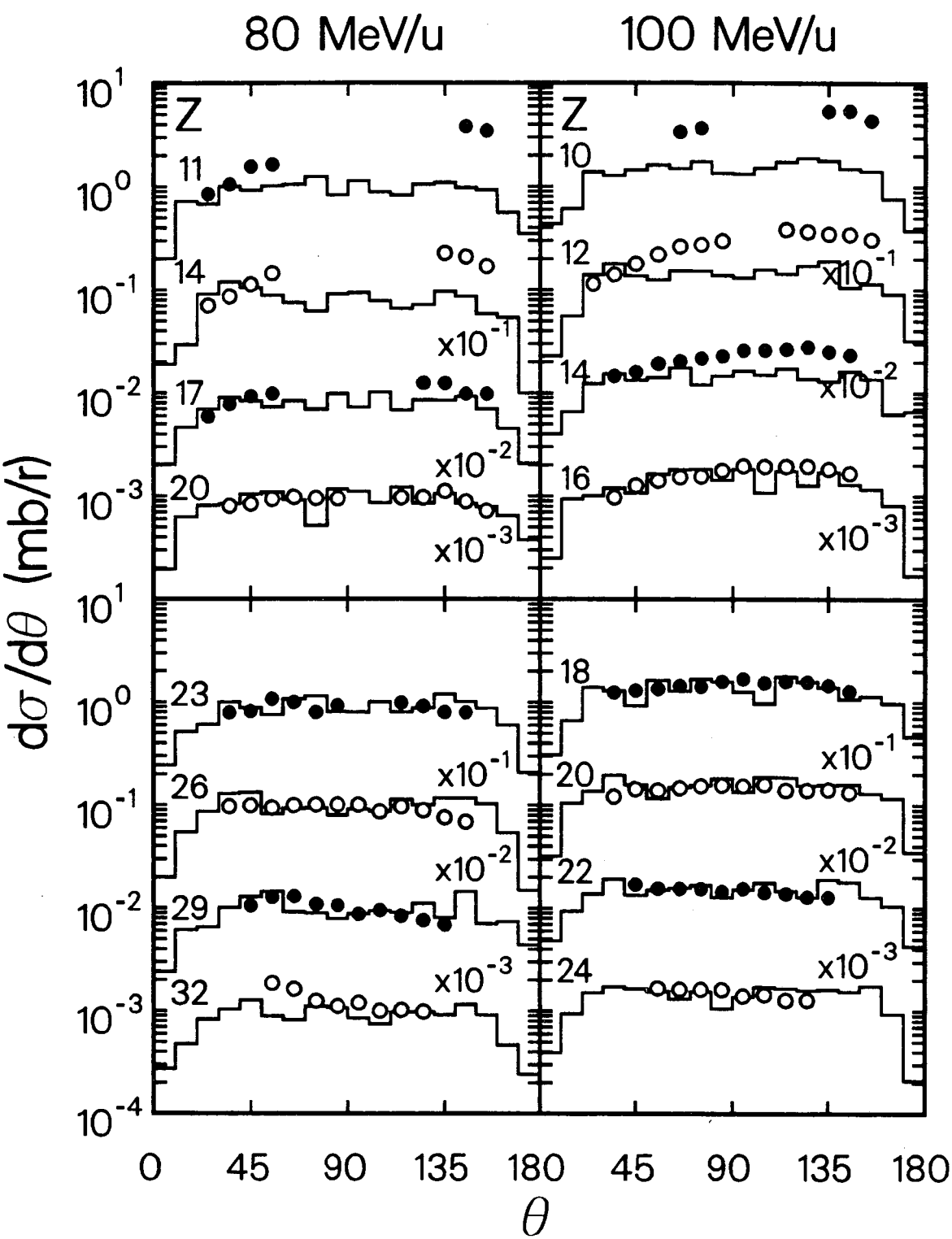

XBL 905-1601

Figure 24

LAWRENCE BERKELEY LABORATORY
UNIVERSITY OF CALIFORNIA
INFORMATION RESOURCES DEPARTMENT
BERKELEY, CALIFORNIA 94720